Petroleum Science 21 (2024) 286–301

Contents lists available at ScienceDirect

Petroleum Science

journal homepage: www.keaipublishing.com/en/journals/petroleum-science

Original Paper

A hybrid physics-informed data-driven neural network for CO_2 storage in depleted shale reservoirs

Yan-Wei Wang [a, b, c], Zhen-Xue Dai [a, b, *], Gui-Sheng Wang [d], Li Chen [e], Yu-Zhou Xia [a, b], Yu-Hao Zhou [f, g, **]

[a] College of Construction Engineering, Jilin University, Changchun, 130026, Jilin, China
[b] Institute of Intelligent Simulation and Early Warning for Subsurface Environment, Jilin University, Changchun, 130026, Jilin, China
[c] School of Energy Resources, China University of Geosciences, Beijing, 100083, China
[d] Department of Safety, Environmental Protection and Quality Management, Shengli Oilfield, Sinopec, Dongying, 257000, Shandong, China
[e] Key Laboratory of Thermo-Fluid Science and Engineering of MOE, School of Energy and Power Engineering, Xi'an Jiaotong University, Xi'an, 710049, Shaanxi, China
[f] College of Computer Science and Technology, China University of Petroleum (East China), Qingdao, 266580, Shandong, China
[g] Department of Physics, University of Fribourg, Fribourg, 1700, Switzerland

ARTICLE INFO

Article history:
Received 13 February 2023
Received in revised form
25 August 2023
Accepted 28 August 2023
Available online 29 August 2023

Edited by Yan-Hua Sun

Keywords:
Deep learning
Physics-informed data-driven neural network
Depleted shale reservoirs
CO_2 storage
Transport mechanisms

ABSTRACT

To reduce CO_2 emissions in response to global climate change, shale reservoirs could be ideal candidates for long-term carbon geo-sequestration involving multi-scale transport processes. However, most current CO_2 sequestration models do not adequately consider multiple transport mechanisms. Moreover, the evaluation of CO_2 storage processes usually involves laborious and time-consuming numerical simulations unsuitable for practical prediction and decision-making. In this paper, an integrated model involving gas diffusion, adsorption, dissolution, slip flow, and Darcy flow is proposed to accurately characterize CO_2 storage in depleted shale reservoirs, supporting the establishment of a training database. On this basis, a hybrid physics-informed data-driven neural network (HPDNN) is developed as a deep learning surrogate for prediction and inversion. By incorporating multiple sources of scientific knowledge, the HPDNN can be configured with limited simulation resources, significantly accelerating the forward and inversion processes. Furthermore, the HPDNN can more intelligently predict injection performance, precisely perform reservoir parameter inversion, and reasonably evaluate the CO_2 storage capacity under complicated scenarios. The validation and test results demonstrate that the HPDNN can ensure high accuracy and strong robustness across an extensive applicability range when dealing with field data with multiple noise sources. This study has tremendous potential to replace traditional modeling tools for predicting and making decisions about CO_2 storage projects in depleted shale reservoirs.

1. Introduction

Because of the harmful effects of greenhouse gases on climate, energy-related CO_2 emissions have become a severe environmental issue worldwide, with far-reaching implications for the simultaneous and sustainable development of society, ecology, and economy (Cai et al., 2021; Mora et al., 2018; Xiao et al., 2022). With global anthropogenic CO_2 emissions having reached an all-time high of 330 billion tons in 2021, dozens of countries and regions have proposed "emission peak" and "carbon neutrality" climate goals to realize the long-term vision of an environment-friendly and carbon-free future (Chen et al., 2022; Jeffry et al., 2021). Carbon capture, utilization, and storage (CCUS)—which transforms the traits of CO_2 from "harm in the sky" to "treasure in the ground"—has become a critical technology for controlling and reducing large-scale industrial greenhouse gas emissions by using decarbonization devices to collect and transport large volumes of

* Corresponding author. College of Construction Engineering, Jilin University, Changchun 130026, Jilin, China.
** Corresponding author. College of Computer Science and Technology, China University of Petroleum (East China), Qingdao, 266580, Shandong, China.
E-mail addresses: dzx@jlu.edu.cn (Z.-X. Dai), yuhao.zhou@unifr.ch (Y.-H. Zhou).

https://doi.org/10.1016/j.petsci.2023.08.032

Nomenclature

C	Concentration, sm^3/m^3
C_D	Wellbore storage factor, dimensionless
C_g	Gas compressibility, MPa^{-1}
D_E	Effective diffusion coefficient, m^2/s
D_K	Knudsen diffusion coefficient, m^2/s
D_M	Molecular diffusion coefficient, m^2/s
f	Content, dimensionless
h	Formation thickness, m
H	Solubility coefficient, $m^3/(Pa\cdot m^3)$
K	Permeability, D
L	Loss function
M	CO_2 storage capacity, m^3
M_g	Molar mass, g/mol
p	Pressure, MPa
p_L	Langmuir pressure, MPa
q	Injection rate, m^3/d
r	Radius, m
R_o, R_k, R_m	Radii of organic particle, kerogen, and matrix, m
R_{SRV}, R_e	Radii of SRV region and external region, m
S	Skin factor, dimensionless
t	Time, h
T	Temperature, K
V_L	Langmuir volume, m^3
w	Hydraulic fracture width, m
x, y, z	Cartesian coordinate, m

Greek symbols

α	Slip coefficient, dimensionless
β	Shape factor, dimensionless
ϕ	Porosity, dimensionless
ω	Reservoir factor vector
γ	Permeability modulus, Pa^{-1}
μ	Viscosity, mPa·s
σ	Standard deviation
ρ	Density, kg/m^3
ε	Relative error
λ	Inter-porosity flow coefficient
ξ_{hf}	Hydraulic fracture half-length, m

Subscripts

c	Clay minerals
er	Exterior region
f	Natural fracture
g	Gas
hf	Hydraulic fracture
i	Initial condition
k	Kerogen
m	Shale matrix
o	Organic matter
SRV	SRV region
w	Wellbore

Abbreviations

CCUS	Carbon capture, utilization, and storage
DeLISA	Deep learning based iteration scheme approximation
FCNN	Fully connected neural network
HPDNN	Hybrid physics-informed data-driven neural network
IELM	Improved extreme learning machine
LNN	Legendre neural network
L-IELM	Legendre improved extreme learning machine
PDEs	Partial differential equations
PINN	Physics-informed neural network
SRV	Stimulated reservoir volume
SEM	Standard error of mean

CO_2 from its sources to secure geological reservoirs for secondary utilization or storage (Chen et al., 2022; Yan and Zhang, 2019). CO_2 storage options include geological formations such as saline aquifers in deep sea areas, unrecoverable coal seams, and depleted oil or gas reservoirs (Dai et al., 2020; Goodman et al., 2020; Jia et al., 2022a; Kou et al., 2021; Xie et al., 2023).

In recent years, depleted reservoirs have been regarded as desirable geological structures for CO_2 sequestration in that the essential infrastructures (including surface facilities, injection/production wells, and transportation facilities) do not require the huge costs of additional construction, in addition to prominent geological features for storage safety and significant storage capacity (Chu et al., 2023; Gao et al., 2022; Zhang et al., 2022b). Moreover, unconventional reservoirs, especially depleted shale reservoirs with sealing caprocks and abundant micro- and nano-scale pore-throat structures, have promising storage potential and sequestration security due to the higher specific surface area and rich organic matter characteristics (Feng et al., 2020; Sun et al., 2020; Zhang et al., 2022a). In addition, the shale matrix has a greater affinity for CO_2 than methane, meaning that CO_2 will be preferentially adsorbed in the nanopores while facilitating methane desorption from the particle surface, thus generating interest in CO_2 sequestration while enhancing the oil/gas recovery (Jia et al., 2019; Zhou et al., 2019). However, accurate characterization of CO_2 transport and storage processes in shale reservoirs remains challenging due to the complex petrophysical properties of shale formations (Wang et al., 2023). Gas transport properties are influenced by shale microstructure, composition as well as flow regimes, thus the complex multi-scale structure hinders the prediction of CO_2 transport in shale and the evaluation of reservoir CO_2 storage capacity, which is essential for the implementation of CO_2 storage engineering projects in depleted shale reservoirs (Kou et al., 2022).

The long-term stable storage of CO_2 injected into depleted shale reservoirs inevitably involves special geological issues that are different from those of conventional hydrocarbon reservoirs, including the complicated transport and storage mechanisms of CO_2 (Tayari and Blumsack, 2020). During CO_2 sequestration in shale reservoirs, CO_2 exists in the multiscale medium system of shale in various storage forms, including free gas, dissolved gas, and adsorbed gas (Chu and Zhang, 2023; Jia et al., 2022a). Free gas refers to CO_2 stored in the pore space of the shale, including micro- and nano-pores, natural fractures and hydraulic fractures (Gao et al., 2022). Adsorbed gas represents CO_2 adsorbed on the pore walls of shale, mostly on the surface of kerogen due to the high affinity, but also partially on the surface of clay minerals (Gou and Xu, 2019; Klewiah et al., 2020). At the same time, due to the strong interaction between kerogen and CO_2, kerogen bulk can be considered as an important storage vessel into which CO_2 molecules diffuse and can be deposited in the form of dissolved gas (Lyu et al., 2021). Various sequestration forms and multi-scale media systems, especially those containing abundant nanoscale pores, result in a strong coupling of multi-scale multi-physicochemical processes with discontinuous behaviors during CO_2 storage in depleted shale reservoirs.

CO_2 storage in shale formations involves complex multi-scale

physicochemical transport processes (Afagwu et al., 2022). Shale formations have the characteristics of tight and ultra-low permeability, usually requiring the application of multi-stage hydraulic fracturing techniques to facilitate the formation of a multi-scale system consisting of organic matter (kerogen), inorganic matter (clay minerals, calcite, pyrite, quartz), natural fractures, and hydraulic fractures for effective shale-reservoir development (Wang et al., 2020). Therefore, the migration of CO_2 in depleted shale formations consists of several stages: Darcy flow in hydraulic fractures and natural fractures, slip flow and transition flow in micro- and nano-pores, adsorption and desorption of clay minerals and kerogen, solid diffusion in organic matter, and Knudsen diffusion in nanopores (Javadpour et al., 2021). Accurate description of integrated CO_2 migration mechanisms in shale is an essential prerequisite for formation parameter inversion and carbon storage capacity (Shen et al., 2022). Accurate prediction of CO_2 injection performance—based on the reservoir information, boundary conditions, and well characteristics that determine carbon sequestration capacity—has enormous implications for the economic evaluation and field implementation of CO_2 sequestration projects (Xu et al., 2021a). However, the establishment of CO_2 geological storage model integrated with multiple transport and storage mechanisms is one of the necessary prerequisites for accurately predicting the dynamic characteristics and determining the carbon sequestration capacity.

Modeling and predicting transport processes in multi-physics and multi-scale systems remains an ongoing scientific problem (Karniadakis et al., 2021; Zhang et al., 2023). The CO_2 storage in depleted shale reservoirs is a uniquely complex system, the dynamics of which are governed by an intricate interplay of physical and chemical processes on temporal and spatial scales spanning 17 orders of magnitude (Feng et al., 2018; Iddphonce et al., 2020). It is generally known that partial differential equations (PDEs) have a major contribution to the description of physicochemical phenomena; however, there are very few cases where PDEs have easily obtainable analytical solutions (Chen et al., 2021; Feng et al., 2021). The PDEs applied in the multi-scale model of CO_2 storage in depleted shale reservoirs cannot provide analytical solutions under the corresponding boundary conditions (Wang et al., 2020). Therefore, various physics-based methods, such as finite difference, finite element, and finite volume, have been established to approximate analytical solutions capable of illustrating complex practical problems employing deduction, for which the ultimate objective is to make them intelligible to users (Steiner, 2022). Traditional discretization methods that usually involve tedious meshing and discretization into iterative solutions for large sparse nonlinear systems have the advantage of solid theoretical analysis (Nicolas et al., 2022). However, the controlling equations for CO_2 storage in strongly heterogeneous shale reservoirs are multivariate, multi-scale, and highly-dimensional; consequently, the prediction of injection dynamics and reservoir parameter inversion for CO_2 sequestration using physics-based methods is time-consuming and laborious.

More specifically, the parameter inversion of shale reservoirs—a reverse modeling process—also occupies a significant place in CO_2 storage implementation; indeed, its inherently unique solutions pose the greatest challenge to the accuracy of inversion results (Xu et al., 2021b). There are many sources of non-unique solutions for reservoir parameter inversion, such as data errors, human manipulation, and the uncertainty of the inversion process, which are equally substantial sources of uncertainty (Alguliyev et al., 2022). With the increment of uncertain factors and complexity of the inverse problem, there are inevitably drawbacks such as slow and low accuracy of curve fitting, which may be unreliable due to human factors or data noise, so the problem of non-unique solutions becomes serious (Wang et al., 2021b). In order to accurately invert reservoir parameters based on production data, automatic history fitting estimation methods are receiving increasing attention (Zhou and Wang, 2022). Probability estimation methods such as the Bayesian, Markov chain Monte Carlo, and Ensemble Kalman filter are also extensively applied in parameter inversion because of their excellent stability (Zhan et al., 2022). However, the above approaches are heavily influenced by the preliminary value assigned, resulting in lower operational efficiency and not effective in solving the problem of non-unique solutions.

In contrast, recently emerging deep learning techniques can extract key features concealed in complex multi-source data, thus solving the high-complexity and high-uncertainty problems—namely, automatically predicting the production and injection dynamics of shale reservoirs and performing the dynamic inversion of reservoir parameters (Liu et al., 2021; Ray et al., 2021; Wang et al., 2021c). Xue et al. proposed a pressure-transient data-driven framework combining random forest and Kalman filtering methods to estimate the aquifer/reservoir properties of natural gas reservoirs and accurately identify water intrusion patterns (Xue et al., 2022a). Dong et al. established an automatic interpretation model of well-test data using a one-dimensional convolutional neural network that can automatically identify the curve type and invert the relevant formation parameters (Dong et al., 2022). Li and Misra proposed a reinforcement learning algorithm based on deep Q-networks and continuous deep deterministic policy gradients for the automatic history matching of numerical reservoir models (Li and Misra, 2021). In general, CO_2 sequestration processes in depleted shale reservoirs can be efficiently assessed by deep learning networks (data-driven models), but the inference transport mechanisms are not yet fully comprehended and explained by physicochemical equations. Consequently, they are opaque to users and the acquisition of high-quality datasets is both time-consuming and resource-intensive, emphasizing the significance of architecting data analysis-prediction systems that combine physics-based and data-driven models.

Powerful deep-learning frameworks enable us to solve arbitrarily complex problems by increasing computational resources; indeed, significant progress has been made in the physics-informed neural network (PINN) model (Tang et al., 2022). Yang et al. proposed the Legendre improved extreme learning machine (L-IELM) method to solve elliptic PDEs by combining the Legendre neural network (LNN) and improved extreme learning machine (IELM) algorithms (Yang et al., 2020). Li et al. proposed a deep learning based iteration scheme approximation (DeLISA) framework; a neural network is then used to approximate an iterative format that integrates the physical information of the governing equations with time to finally solve high-dimensional PDEs (Li et al., 2022b). In addition, Raissi et al. proposed a deep-learning based hidden fluid mechanics capable of encoding critical physical laws governing fluid motion to solve the forward and backward problems associated with PDEs (Raissi et al., 2020). Therefore, physics-informed deep neural network can obtain physically consistent solutions by introducing physical biases into the training samples, model architecture, and reasoning algorithms of data-driven models, whereas the optimization of data-driven models can be constrained by PDEs to significantly improve the speed of neural network convergence.

In summary, it is essential to incorporate physics with data-driven approaches by introducing and integrating a PINN to accelerate the convergence of the entire network, thereby insuring the interpretability, transparency, and high accuracy of the data analysis-prediction systems to achieve highly autonomous and error-free operation for CO_2 transport and storage in depleted shale reservoirs. In this study, we developed an integrated multi-scale

model involving strongly non-homogeneous media systems to characterize the CO_2 storage in depleted shale reservoirs. On this basis, we proposed an innovative hybrid physics-informed data-driven neural network (HPDNN) model that can be generated with a limited number of simulation runs and can significantly accelerate the forward and inversion processes by incorporating physical principles (PDEs, boundary/initial conditions) and practical theories (engineering regulation and expert experience), enabling the prediction of CO_2 injection dynamics and accurate inversion of reservoir parameters, as well as estimating the CO_2 storage capacity of shale reservoirs. Furthermore, to evaluate the application performance of the HPDNN, several cases of CO_2 sequestration in shale were designed to evaluate the extrapolation ability of the model to field application scenarios with different noise factors. We demonstrated that the HPDNN is capable of solving the time-consuming and labor-intensive challenges of numerical simulations and accurately assesses multi-scale CO_2 sequestration in depleted shale reservoirs with strong heterogeneity.

2. Methodology

2.1. Establishment of numerical model

This section presents the establishment of the numerical model for CO_2 storage in depleted shale reservoirs, considering systems with different scales. The proposed multi-scale model—constructed with a commercial numerical simulator (COMSOL Multiphysics) using parameters derived from actual reservoirs—are employed to generate CO_2 injection performance data as an information base used to train the deep learning model. This model can intelligently predict injection performance, perform reservoir parameter inversion, and evaluate CO_2 sequestration capacity under different conditions. Specifically, the injection results that were generated and the partial parameter distributions during the injection process were assembled into a comprehensive knowledge base, from which hybrid acceleration training and verification of the model were performed with the neural network system for solving PDEs. Details of the physical model, reservoir grid, PDEs, and selection of the basic parameters are provided.

2.1.1. Physical model

Shale gas reservoirs that have been developed by horizontal wells are composed of heterogeneous and anisotropic porous systems, typically containing organic matter (nanoscale), porous kerogen (microscale), clay minerals (microscale), inorganic matrix (mesoscale), natural fractures (mesoscale) and hydraulic fractures (mesoscale), such that the injected CO_2 involves multiple transport and sequestration mechanisms in depleted shale formations (macroscale), the schematic diagram of which is shown schematically in Fig. 1. The injected CO_2 is transported in the above multi-scale systems and extensively distributed in the nanoscale and microscale pores of the shale matrix, and eventually stored in different forms such as dissolved gas (CO_2 dissolved inside organic matter particles, not considering dissolved in oil and water in this paper), adsorbed gas (porous kerogen and clay minerals), and free gas (micro-nanopores and fractures). Various storage forms, particularly in systems involving a large number of nanoscale pores, lead to coupled multiscale multiple transport mechanisms as follows: (1) transport of ground-injected CO_2 from the horizontal wellbore to the reservoir system; (2) gas migration from the fracture network to the shale matrix mainly by Darcy flow; (3) slip flow in the pore network and adsorption to clay particles in the inorganic matrix system; (4) slip flow in the nanopores and adsorption to organic particles in the kerogen system; (5) gas on the surface of nanopores migrates by solid diffusion to form dissolved gas inside the organic particles caused by the concentration difference. On this basis, the physical model of sequestration in depleted shale reservoirs is established, as shown in Fig. 2. The near-well area where a horizontal well exists in the center has been repeatedly fractured and SRV to form a fracture network different from the conventional two-wing fractures, prompting the hydraulic fractures to interconnect with the natural fractures, while forming an internal region with high permeability. Therefore, shale reservoirs with the external closed boundary typically contain hydraulic fractures with finite conductivity, natural fractures, and the SRV region. For most CO_2 sequestration processes, the injected CO_2 is in supercritical state due to high reservoir temperature and pressure. Other assumptions of the proposed model are presented as follows.

- Reservoir fluids other than CO_2 in the depleted shale formation are ignored (Shen et al., 2023).
- The content of dissolved gas is characterized by Henry's law, while the transport of the dissolved gas is governed by Fick's diffusion law (He et al., 2016).
- Permeability of inorganic matrix system and kerogen system is modified by slippage effects (Cui et al., 2022).
- The transport of CO_2 contains multiple forms of intertwined diffusive flows, including molecular diffusion and Knudsen diffusion, so that the effective diffusion coefficient (D_E) is introduced as (Jeon et al., 2014; Lucas et al., 2004):

$$\frac{1}{D_E}=\frac{1}{D_M}+\frac{1}{D_K} \tag{1}$$

where D_M refers to molecular diffusion coefficient; and D_K indicates Knudsen diffusion coefficient.

- The depleted shale formation has a constant temperature T (Kou et al., 2021).
- Since the variation of reservoir pressure affects the permeability performance of natural fractures, the stress-sensitive effect should be taken into account (Afagwu et al., 2020).
- Effects of gravity and capillary pressure are neglected (Chu et al., 2019b).

2.1.2. Reservoir grid

A commercial numerical simulator—COMSOL Multiphysics®—is used to simulate the proposed model of realistic CO_2 sequestration processes in depleted shale formations by solving PDEs via the finite element method. A multi-fractured horizontal well is arranged in the center of a cylindrical depleted shale reservoir with a radius of 3000 m, which constitutes the research object of this study, as shown in Fig. 3. In addition, our numerical model includes established PDEs to describe the CO_2 adsorption, diffusion, dissolution, Darcy flow, and slip flow in different systems at multiple scales. An unstructured grid technique is used to establish irregular hydraulic fractures. And a local grid refinement methodology is used to enhance the reliability of the numerical simulation results. Furthermore, the time step of the pre-injection stage is set smaller than that of the post-injection stage to improve computational efficiency.

2.1.3. Governing equations

According to the above physical model and assumptions made according to the actual situation, the multi-scale governing equations (PDEs) considering CO_2 diffusion, dissolution, adsorption/desorption, slip flow, and Darcy flow are established for CO_2 sequestration in depleted shale reservoirs (Fig. 2). Depleted shale reservoirs typically involve two regions: the SRV region and the

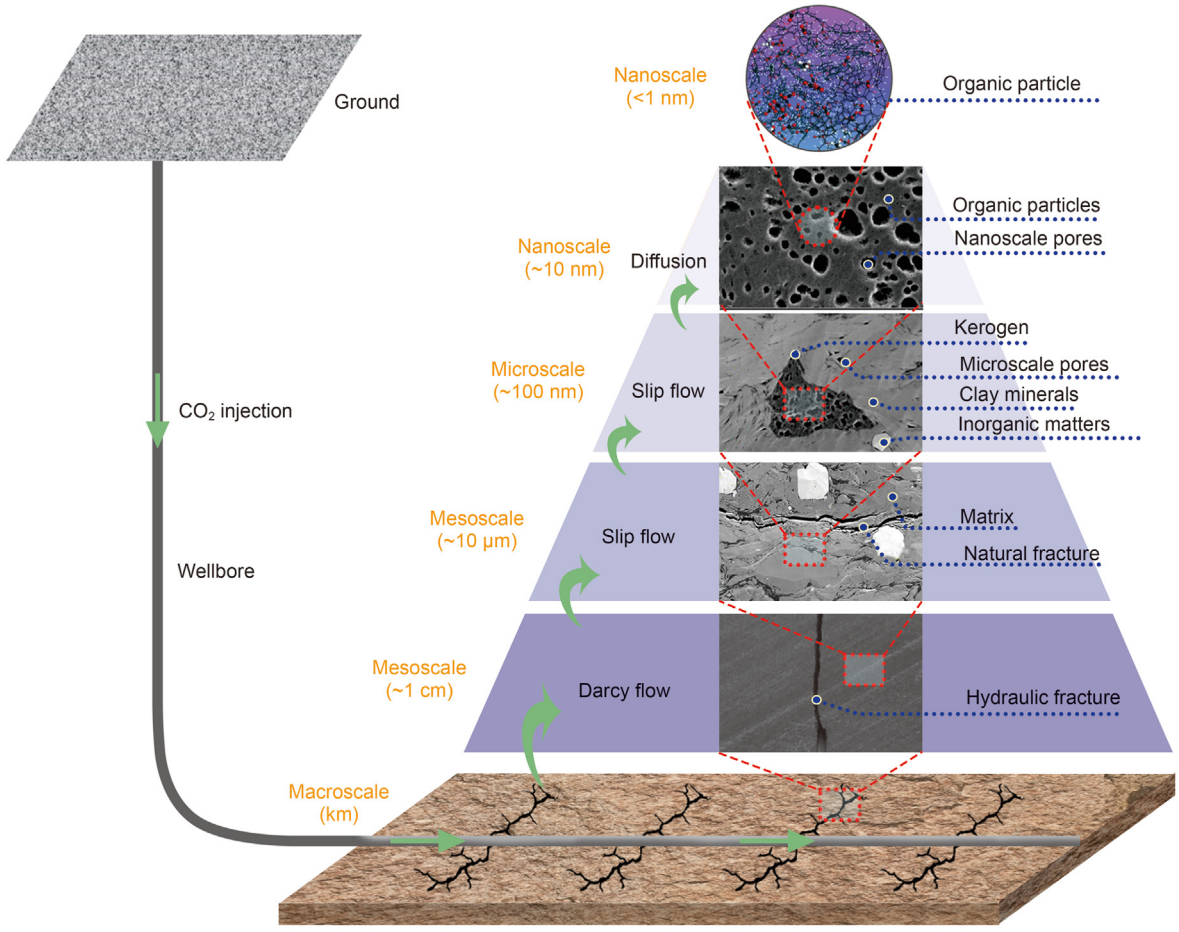

Fig. 1. The schematic diagram of CO_2 transport and sequestration in depleted shale reservoirs (modified from Wang et al., 2023).

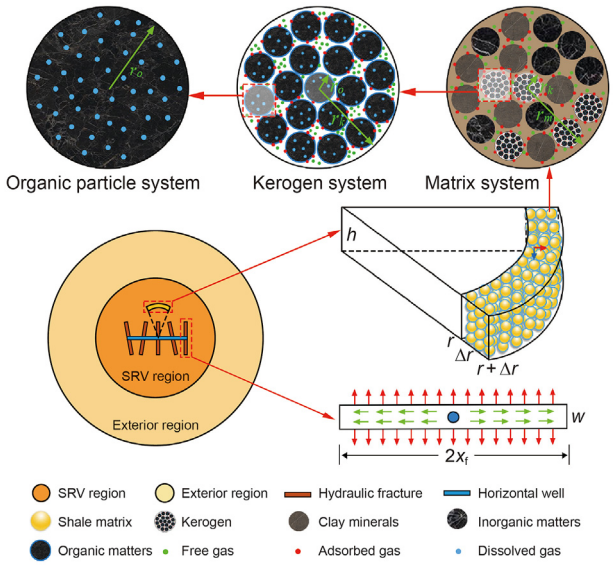

Fig. 2. The physical model of CO_2 transport and sequestration in depleted shale reservoirs.

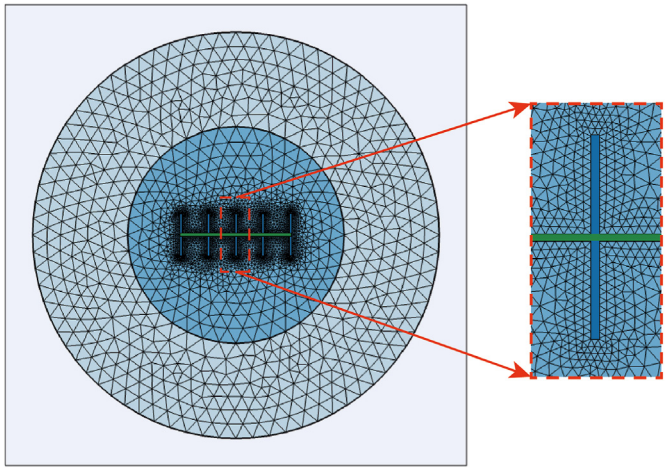

Fig. 3. The numerical model of CO_2 sequestration in depleted shale reservoirs.

original formation, containing organic matter, porous kerogen, inorganic matrix, and fractures. The detailed mathematical model for CO_2 sequestration in the depleted shale reservoir is shown in this section.

2.1.3.1. SRV region of the depleted shale reservoir

2.1.3.1.1. Organic particle system. Because of the high affinity of CO_2 molecule to organic matter, it is easy to dissolve in solid organic matter (Huang et al., 2021). Considering the extremely low

permeability of organic matter in shale, it can be assumed that CO_2 dissolved in shale organic matter is driven by concentration differences rather than by pressure gradients, implying that the transport process of dissolved gas in organic matter is controlled by the combination of molecular diffusion and Knudsen diffusion (Chu et al., 2019a). Therefore, the continuity equation for the organic particle system can be obtained (He et al., 2016):

$$\frac{1}{r_o^2}\frac{\partial}{\partial r_o}\left(r_o^2\rho_o\beta_o D_E\frac{\partial C_o}{\partial r_o}\right)=\rho_o\frac{\partial C_o}{\partial t} \tag{2}$$

where C_o refers to the concentration of CO_2; β_o is the shape factor of the organic particles; and r_o is the radius of the organic medium. (Please see the Nomenclature section for a complete list of definitions for the symbols used throughout all equations.) The initial and boundary conditions can be written:

$$C_{r_o=R_o,r_k}=Hp_k|_{r_k}\ \text{External boundary condition} \tag{3}$$

$$\left.\frac{D_E\rho_o\beta_o r_o^2}{0.941\times10^{-3}}\frac{\partial C_o}{\partial r_o}\right|_{r_{o\to0}}=0\ \text{Internal boundary condition} \tag{4}$$

$$C|_{t=0}=C_i=Hp_i\ \text{Initial condition} \tag{5}$$

2.1.3.1.2. Kerogen system. Kerogen contain an abundant amount of nanopores with high specific surface area, which is the main storage space for CO_2 in shale. The injected gas can be stored in the porous kerogen in a variety of states, involving adsorbed gas on the surface of organic particles, free gas in organic nanopores, and gas migrating into organic particles by diffusion. Therefore, the mass conservation equation for the porous kerogen system is formulated (Wang et al., 2023):

$$\begin{aligned}&\frac{1}{r_k^2}\frac{\partial}{\partial r_k}\left(r_k^2\rho_k\frac{3.6\beta_k\alpha_k K_{ki}}{\mu}\frac{\partial p_k}{\partial r_k}\right)-\rho_k\frac{V_{Lk}p_k}{(p_k+p_{Lk})^2}\frac{\partial p_k}{\partial t}\\&-\left(1-\frac{\phi_k}{f_k}\right)\frac{3}{R_o}\rho_o\beta_o D_E\left.\frac{\partial C_o}{\partial r_o}\right|_{r_o=R_o,r_k}\\&=\frac{\partial}{\partial t}\left(\frac{p_k M_g C_{gk}\phi_k}{ZRTf_k}\right)\end{aligned} \tag{6}$$

where α_k is the permeability correction coefficient considering the slip flow effect (Afagwu et al., 2022; Liehui et al., 2019); β_k represents the shape factor, expressed as follows:

$$\alpha_k=\frac{K_k}{K_{ki}}=\left[1+\frac{128Kn\arctan(4Kn^{0.4})}{3\pi^2(1-4/b)}\right]\left[1+\frac{4Kn}{1-bKn}\right] \tag{7}$$

$$\beta_k=4\left(\frac{1}{x_k^2}+\frac{1}{y_k^2}\right) \tag{8}$$

where K_{ki} denotes the absolute permeability of kerogen; K_k represents the apparent permeability of kerogen. The initial and boundary conditions can be written:

$$p_k|_{r_k=R_k,r_m}=p_m|_{r_m}\ \text{External boundary condition} \tag{9}$$

$$\left.\frac{\rho_k\beta_k\alpha_k K_{ki}r_k^2}{0.941\times10^{-3}\mu}\frac{\partial p_k}{\partial r_k}\right|_{r_{k\to0}}=0\ \text{Internal boundary condition} \tag{10}$$

$$p_k|_{t=0}=p_i\ \text{Initial condition} \tag{11}$$

2.1.3.1.3. Inorganic matrix system. The shale matrix system is mainly composed of porous kerogen and clay minerals. The injected gas can be stored in the inorganic matrix in various states, involving adsorbed gas on the surface of clay mineral particles, free gas in inorganic micropores, and gas migrated into kerogen in consideration of slip effects. Therefore, the mass conservation equation for the inorganic matrix system is formulated (Wang et al., 2023):

$$\begin{aligned}&\frac{1}{r_m^2}\frac{\partial}{\partial r_m}\left(r_m^2\rho_m\frac{3.6\beta_m\alpha_m K_{mi}}{\mu}\frac{\partial p_m}{\partial r_m}\right)-\rho_m f_c\frac{V_{Lc}p_m}{(p_m+p_{Lc})^2}\frac{\partial p_m}{\partial t}\\&-\frac{10.8}{R_k}\rho_k f_k\beta_k\frac{K_k}{\mu}\left.\frac{\partial p_k}{\partial r_k}\right|_{r=R_k,r_m}\\&=\frac{\partial}{\partial t}\left(\frac{p_m M_g C_{gm}\phi_m}{ZRT}\right)\end{aligned} \tag{12}$$

where α_m is the permeability correction coefficient introduced by considering the slip flow effect, expressed as follows (Afagwu et al., 2022; Liehui et al., 2019):

$$\alpha_m=\frac{K_m}{K_{mi}}=\left[1+\frac{128Kn\arctan(4Kn^{0.4})}{3\pi^2(1-4/b)}\right]\left[1+\frac{4Kn}{1-bKn}\right] \tag{13}$$

where K_{mi} denotes the absolute permeability of the shale matrix, and K_m represents the apparent permeability of the shale matrix. The initial and boundary conditions can be written:

$$p_m|_{r_m=R_m,r}=p_{ir}|_r\ \text{External boundary condition} \tag{14}$$

$$\left.\frac{\rho_m\beta_m\alpha_m K_{mi}r_m^2}{0.941\times10^{-3}\mu}\frac{\partial p_m}{\partial r_m}\right|_{r_{m\to0}}=0\ \text{Internal boundary condition} \tag{15}$$

$$p_m|_{t=0}=p_i\ \text{Initial condition} \tag{16}$$

2.1.3.1.4. Natural fracture system. Natural fractures are one of the important components in shale reservoirs, performing an essential contribution to storing and transporting CO_2. Therefore, the continuity equation for the natural fracture system in the SRV region can be obtained (Chu et al., 2019a):

$$\begin{aligned}&\frac{3.6}{r}\frac{\partial}{\partial r}\left(r\rho_{ir}\frac{K_{1fi}e^{-\alpha(p_i-p_{ir})}}{\mu}\frac{\partial p_{ir}}{\partial r}\right)-\frac{10.8}{R_m}\rho_m\beta_m\frac{K_m}{\mu}\left.\frac{\partial p_m}{\partial r_m}\right|_{r=R_m,r}\\&=\frac{\partial}{\partial t}\left(\frac{p_{ir}M_g C_{gir}\phi_{fir}}{ZRT}\right)\end{aligned} \tag{17}$$

The initial and boundary conditions can be written:

$$\begin{cases}p_{ir}|_{r=r_{SRV}}=p_{er}|_{r=r_{SRV}}\\\left.\dfrac{\partial p_{ir}}{\partial r}\right|_{r=r_{SRV}}=\dfrac{1}{M_{12}}\left.\dfrac{\partial p_{er}}{\partial r}\right|_{r=r_{SRV}}\end{cases}\ \text{External boundary condition} \tag{18}$$

$$\left.\frac{K_{\mathrm{irfi}}\mathrm{e}^{-\alpha(p_{\mathrm{i}}-p_{\mathrm{ir}})}rh}{1.842\times10^{-3}\mu}\frac{\partial p_{\mathrm{ir}}}{\partial r}\right|_{r=r_{\mathrm{w}}}=-q_{\mathrm{sc}}B \text{ Internal boundary condition} \tag{19}$$

$$p_{\mathrm{ir}}|_{t=0}=p_{\mathrm{i}} \text{ Initial condition} \tag{20}$$

2.1.3.2. Hydraulic fracture system. For the mass transfer within hydraulic fractures surrounded by the porous media of shale (on the basis of previous assumptions), hydraulic fractures are intimately connected to natural fractures and inorganic matrix, so the governing equation of CO_2 transport in the hydraulic fracture system with finite-conductivity can be obtained by integrating the mass balance, flow, and state equations, respectively (Kou et al., 2022):

$$\frac{\partial}{\partial\xi}\left(K_{\mathrm{hf}}\frac{p_{\mathrm{hf}}}{\mu Z}\frac{\partial p_{\mathrm{hf}}}{\partial\xi}\right)+\frac{\partial}{\partial\tau}\left(K_{\mathrm{hf}}\frac{p_{\mathrm{hf}}}{\mu Z}\frac{\partial p_{\mathrm{hf}}}{\partial\tau}\right)=\frac{\partial}{\partial t}\left(\frac{\phi_{\mathrm{hf}}C_{\mathrm{ghf}}p_{\mathrm{hf}}}{Z}\right),\quad\left(0\le\xi\le\xi_{\mathrm{f}},\ 0\le\tau\le\frac{w_{\mathrm{hf}}}{2}\right) \tag{21}$$

The interface between the hydraulic fracture system and SRV region does not account for mass loss, so the continuum condition can be expressed formulated in terms of the equivalent production rate as follows:

$$\left.\frac{p_{\mathrm{hf}}T_{\mathrm{sc}}}{p_{\mathrm{sc}}TZ}\frac{K_{\mathrm{hf}}}{\mu}\frac{\partial p_{\mathrm{hf}}}{\partial\tau}\right|_{\tau=w_{\mathrm{hf}}/2}=\left.\frac{p_{\mathrm{ir}}T_{\mathrm{sc}}}{p_{\mathrm{sc}}TZ}\frac{K_{\mathrm{irf}}}{\mu}\frac{\partial p_{\mathrm{ir}}}{\partial\tau}\right|_{\tau=w_{\mathrm{hf}}/2} \tag{22}$$

Due to the large aspect ratio of hydraulic fractures (obvious differences between the length and width of fractures), the CO_2 migration rate at each radial hydraulic fracture was ignored and the following formula was obtained:

$$\left.\frac{\partial p_{\mathrm{hf}}}{\partial\xi}\right|_{\xi=\xi_{\mathrm{f}}}=0 \tag{23}$$

For the mass conservation equation of each hydraulic fracture, the CO_2 injection rate can be obtained:

$$\frac{p_{\mathrm{hf}}T_{\mathrm{sc}}}{p_{\mathrm{sc}}TZ}\frac{K_{\mathrm{hf}}}{\mu}h\int_0^{w_{\mathrm{hf}}/2}\left.\frac{\partial p_{\mathrm{hf}}}{\partial\xi}\right|_{\xi=0}\mathrm{d}\tau=\frac{q_{\mathrm{hf}}}{2} \tag{24}$$

Based on the equation $p_{\mathrm{w}}=p_{hf}\big|_{\xi=0}$, the wellbore injection pressure can be obtained by substituting Eqs. (22)–(24) into Eq. (21), yielding the injection performance curve during CO_2 sequestration in depleted shale reservoirs.

2.1.3.3. Exterior region of the depleted shale reservoir. The external area of the reservoir can be considered as the initial shale formation, unaffected by the reservoir reconstruction. Similarly, the continuity equation governing for the exterior region with impermeable boundary is formulated (Wang et al., 2023):

$$\frac{1}{r}\frac{\partial}{\partial r}\left(r\rho_{\mathrm{er}}\frac{3.6K_{2\mathrm{fi}}\mathrm{e}^{-\alpha(p_{\mathrm{i}}-p_{\mathrm{er}})}}{\mu}\frac{\partial p_{\mathrm{er}}}{\partial r}\right)-\frac{10.8}{R_{\mathrm{m}}}\rho_{\mathrm{m}}\beta_{\mathrm{m}}\frac{K_{\mathrm{m}}}{\mu}\left.\frac{\partial p_{\mathrm{m}}}{\partial r_{\mathrm{m}}}\right|_{r=R_{\mathrm{m}},r}=\frac{\partial}{\partial t}\left(\frac{p_{\mathrm{er}}M_{\mathrm{g}}C_{\mathrm{ger}}\phi_{\mathrm{fer}}}{ZRT}\right) \tag{25}$$

The initial and boundary conditions are represented by Eqs. (26) and (27):

$$\left.\frac{\partial p_{\mathrm{er}}}{\partial r}\right|_{r=r_{\mathrm{e}}}=0 \text{ External boundary condition} \tag{26}$$

$$p_{\mathrm{er}}|_{t=0}=p_{\mathrm{i}} \text{ Initial condition} \tag{27}$$

2.1.3.4. Calculation of CO_2 storage capacity. To obtain CO_2 storage capacity in depleted shale reservoirs, a scope of CO_2 injection rates must be evaluated that consider reservoir physical parameters, geologic conditions, injection equipment requirements, and economic factors, and then a constrained injection pressure can be set for CO_2 injection and storage. Based on the proposed multi-scale model, the CO_2 sequestration capacity can be acquired by the cumulative CO_2 injection volume when the constrained pressure is reached:

$$M=\int_0^{t_{\mathrm{c}}}Q_{\mathrm{in}}\mathrm{d}t \tag{28}$$

where M refers to CO_2 storage capacity; Q_{in} indicates the injection rate of CO_2; t_{c} denotes the injection duration when the constrained pressure is reached.

2.1.4. Basic parameters

The ideal ranges of basic parameters for the numerical simulation are determine from previous publications. The parameters chosen in shale reservoirs should be as diverse as possible to provide users with a variety of mine application options while satisfying the field applications. Each input variable was created randomly according to actual situations. The basic parameters involved in the numerical simulation of CO_2 sequestration in depleted shale reservoirs are shown in Table 1 and can be changed according to the needs of the actual application scenarios. The input parameters of the model are determined according to the actual reservoir data, eliminating the effects of unreasonable input parameters and providing sufficient cases for the training of HPDNN model.

2.2. Neural network structure

In recent years, deep learning has made outstanding contributions to the fields of oilfield development and geological CO_2 storage, such as the prediction of dynamic changes in high-dimensional physical fields and production parameters (Peng et al., 2022; Wang et al., 2021d), reservoir parameter inversion based on automatic history matching (Wang et al., 2021a), and multi-objective optimization of production and storage based on deep reinforcement learning (Hourfar et al., 2019). Compared with traditional physical and numerical simulation techniques for reservoir development and CO_2 storage, deep learning-based methods have a higher prediction accuracy, faster operation speed, and broader application

Table 1
Basic parameters involved in the numerical simulation.

Item	Parameter	Value
Reservoir	Reservoir temperature, K	338.15
	Reservoir thickness, m	20–50
	Depleted pressure, MPa	0.6
	Porosity of natural fractures	0.0045
	Permeability of natural fracture, mD	1×10^{-3}
	Porosity of inorganic matrix	0.045
	Permeability of matrix, mD	1×10^{-5}
	Slip coefficient of matrix	1–5
	Inter-porosity flow coefficient of matrix	10^{-5}–10^{-1}
	Porosity of kerogen	0.001–0.01
	Content of kerogen	0.01–0.1
	Permeability of kerogen, mD	1×10^{-6}
	Slip coefficient of kerogen	1–5
	Inter-porosity flow coefficient of kerogen	10^{-6}–10^{-2}
	Porosity of organic matter	0.025
	Content of clay minerals	0.1–0.5
	Hydraulic fracture half-length, m	20–100
	Permeability of hydraulic fracture, mD	1000
	SRV radius, m	600
	Boundary radius, m	1500–20000
	Mobility ratio	2–20
Well	Well length, m	800
	Well radius, m	0.09144
	Constrained pressure, MPa	5–25
	Wellbore storage	0.1–1
	Skin factor	−0.1–0.1
CO_2	Injection rate, m^3/d	10^4–10^6
	Effective diffusion coefficient, m^2/s	1×10^{-7}–1×10^{-4}
	Compressibility, MPa^{-1}	0.048
	Langmuir volume of kerogen, m^3/m^3	10
	Langmuir pressure of kerogen, MPa	10
	Viscosity, mPa·s	0.01
	Coefficient of compressibility	0.8
	Langmuir volume of clay minerals, m^3/m^3	5
	Langmuir pressure of clay minerals, MPa	10
	Z factor	0.8

scenarios and scope. In this study, we used a deep learning technique to fit the relationship between the parameters of the proposed model and the injection performance results. Therefore, on the basis of the simulation results generated by COMSOL, a deep fully connected neural network (FCNN) was used to fit the relationship between the static and spatiotemporal dynamic reservoir parameters and the injection pressure results.

A schematic of the PINN structure is shown in Fig. 4, containing three functional modules: dynamic prediction of CO_2 injection pressure, inversion of reservoir parameters, and evaluation of CO_2 sequestration capacity. According to Eq. (21), the CO_2 injection pressure is closely related to the intermediate variable known as hydraulic fracture pressure (p_{hf}) and the final target CO_2 storage capacity can be calculated from the injection performance curve. Therefore, the fitting target of the neural network can be changed to hydraulic fracture pressure. If the neural network can accurately fit the variables, the algorithm can effectively predict the dynamic change in the CO_2 injection pressure and accurately evaluate the CO_2 storage capacity. In summary, a fully connected neural network (Φ) needs to be trained to predict the dynamics of CO_2 injection pressure by introducing reservoir factors and spatiotemporal variables:

$$\Phi(\boldsymbol{x}, t, \omega, \theta) \rightarrow u(\boldsymbol{x}, t)|_{\omega} \tag{29}$$

where $\boldsymbol{x}$ refers to the spatial coordinate; ω is the reservoir factor; u is the solution of the PDEs; and θ is the trainable weight of the neural network.

The first layer of the neural network used was the factor-input layer, from which the reservoir properties and engineering parameters in Table 1 and the dynamic spatiotemporal information of the grid were input into the neural network. It is worth noting that the absolute differences between the different parameters are significant; for example, the effective diffusion coefficient holds values in the range of 1×10^{-7} to 1×10^{-4}, while the boundary radius holds values in the range of 1500–20000, which inevitably has an impact on the training of smaller parameters in the neural network. Furthermore, standardized data are most suitable for the operation of neural networks; therefore, it is necessary to regularize various input parameters as follows (Yang et al., 2019):

$$\boldsymbol{x}_i' = \frac{\boldsymbol{x}_i - \mu(\boldsymbol{x})}{\sigma(\boldsymbol{x})} \tag{30}$$

where $\mu(\boldsymbol{x})$ denotes the mean value and $\sigma(\boldsymbol{x})$ refers to the standard deviation, determined by uniformly random sampling of the training dataset.

As mentioned above, the main goal of the neural network was to fit the simulated data of CO_2 transport and storage based on COMSOL. The process of finite element numerical simulation is complex, especially for proposed model of CO_2 sequestration in depleted shale reservoirs with strong heterogeneity; it involves controlling equations with many factors and complex meshing patterns. Consequently, it is inefficient to calculate and store enough of high-quality training data. On the other hand, deep learning is a data-driven computational technique that outperforms traditional statistical methods in extracting features from ultrahigh-dimensional data (Cai et al., 2022; Li et al., 2022a; Wen et al., 2023). However, the training effectiveness of deep learning networks relies heavily on the quality and quantity of the data (Chen and Lin, 2014; Najafabadi et al., 2015). Therefore, a hybrid training method was used to improve the training efficiency and effectiveness of neural networks bogged down by the aforementioned practical problems.

Previous research has shown that deep FCNN can approximate complex nonlinear physical systems simply by learning physics—i.e., using neural networks to fit solutions to the equations of the physical system, even without observational data as a training set, constituting an efficient and exciting research direction. Compared to complex and tedious analytical methods, neural networks can utilize gradient descent parameter updates to approximate the exact numerical solution to a system of physical equations; moreover, such networks have made progress in solving hydrodynamic problems (Mao et al., 2020; Raissi et al., 2019). Therefore, training neural networks simultaneously using physical knowledge (PDEs) and sampled data is a natural idea for network training acceleration; furthermore, this method of combining physics-informed and data-driven neural networks constitutes a data assimilation algorithm (Wu and Qiao, 2021). Unlike existing studies of data assimilation that primarily aim to solve deterministic equations (i.e., the parameters are single-invariant in the PDE system), the present study used a hybrid training approach to fit the relationship between the system factors and the target results simultaneously. The objective function (loss function) of the entire hybrid training system consists of two parts: 1) loss of the neural network on the sampled data (the result of numerical simulation calculation); and 2) loss of the neural network on the PDE system, consisting of three sub-losses. The PDEs are transformed into residuals using the nonlinear differential operator *F*, with the specific form of the hybrid training represented as follows:

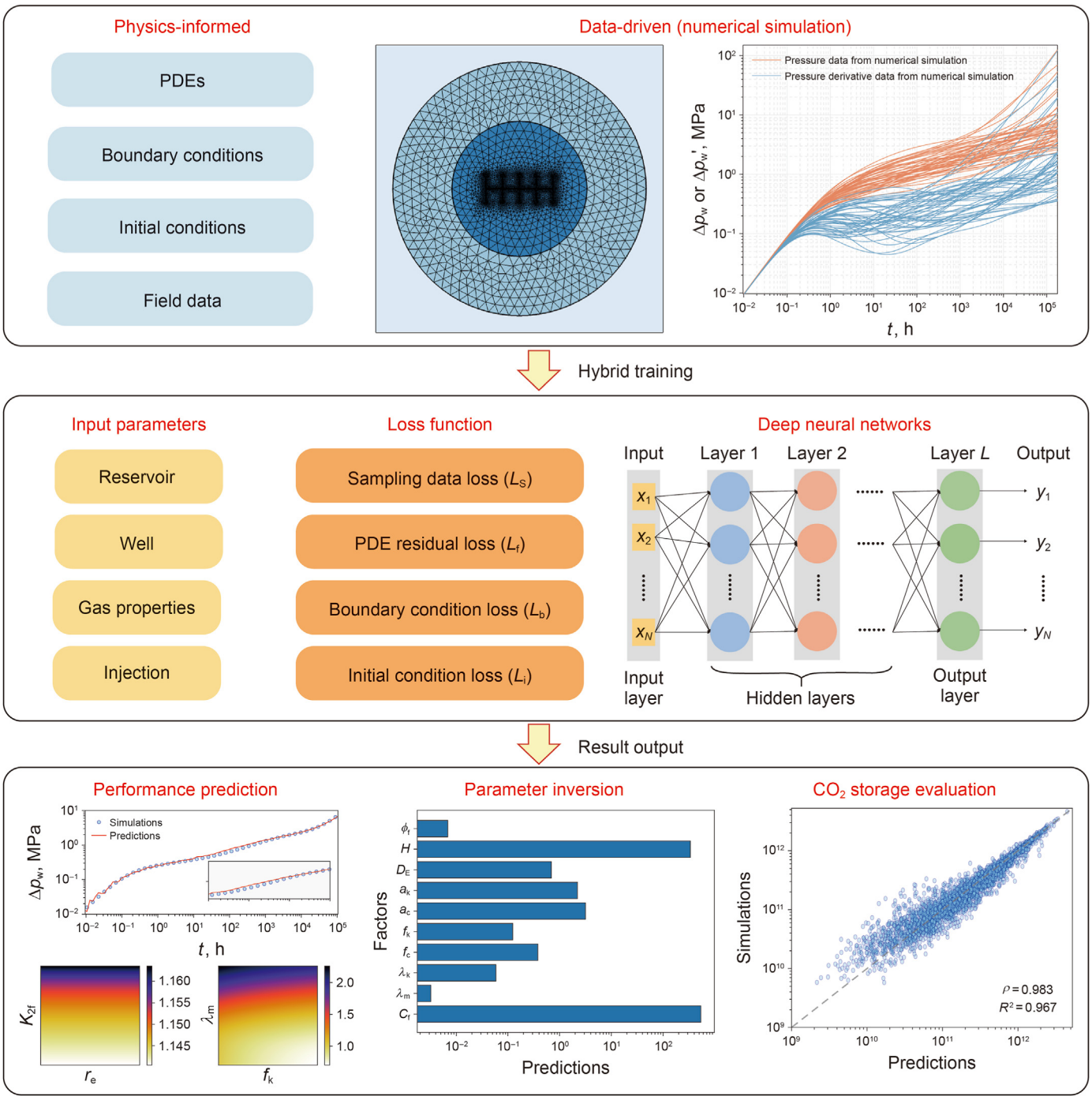

Fig. 4. Schematic diagram of the hybrid physics-informed data-driven neural network (HPDNN) structure.

$$F(\boldsymbol{x}, t, u, \partial_{\boldsymbol{x}} u, \partial_{\boldsymbol{t}} u, \ldots, \omega) = 0,\ \boldsymbol{x} \in \Omega,\ t \in [0, T] \tag{31}$$

where Ω and $\partial\Omega$ represent the spatial domain and boundary, respectively, while u is the solution of the PDEs satisfying boundary condition B and initial condition I:

$$B(\boldsymbol{x}, t, u, \partial_x u, \partial_t u, \ldots, \omega) = 0,\ \boldsymbol{x} \in \partial\Omega,\ t \in [0, T] \tag{32}$$

$$I(\boldsymbol{x}, 0, u, \partial_x u, \ldots, \omega) = 0,\ \boldsymbol{x} \in \Omega \tag{33}$$

The idea of hybrid training is to fit the observed data and solve the system of PDEs simultaneously; the training loss of the neural network can then be written as:

$$L = L_s + \lambda_f \cdot L_f + \lambda_f \cdot L_b + \lambda_i \cdot L_i \tag{34}$$

where L_s is the loss of the neural network on the observed data (sampled data based on numerical simulation results); L_f, L_b, and L_i denote the loss of the neural network on the PDEs, boundary conditions, and initial conditions, respectively; and λ_f, λ_b, and λ_i are the corresponding adjustable weights to assess the proportion and

influence of the physical knowledge. Initially the same weights can be used for all terms, which can then be further adjusted according to the value of loss functions to obtain a more promising performance. The specific forms of the four sublosses are:

$$\begin{cases} \mathscr{L}_{\mathrm{s}}(\theta)=\dfrac{1}{|\Gamma|}\displaystyle\sum_{(\boldsymbol{x},t,\omega)\in\Gamma}\left(\Phi(\boldsymbol{x},t,\omega,\theta)-u(\boldsymbol{x},t)|_{\omega}\right)^2 \\ \mathscr{L}_{\mathrm{f}}(\theta)=\dfrac{1}{|\Gamma|}\displaystyle\sum_{(\boldsymbol{x},t,\omega)\in\Gamma}\left(F(\boldsymbol{x},t,\Phi(\omega\theta),\partial_x\Phi(\omega\theta),\partial_t\Phi(\omega\theta),\ldots,\omega)\right)^2 \\ \mathscr{L}_{\mathrm{b}}(\theta)=\dfrac{1}{|\partial\Gamma|}\displaystyle\sum_{(\boldsymbol{x},t,\omega)\in\theta\Gamma}B(\boldsymbol{x},t,\Phi(\omega,\theta),\partial_x\Phi(\omega,\theta),\partial_t\Phi(\omega,\theta),\ldots,\omega)^2 \\ \mathscr{L}_{\mathrm{i}}(\theta)=\dfrac{1}{|\Gamma|}\displaystyle\sum_{(\boldsymbol{x},0,\omega)\in\Gamma}I(\boldsymbol{x},0,\Phi(\omega,\theta),\partial_x\Phi(\omega,\theta),\ldots,\omega)^2 \end{cases} \tag{35}$$

where Γ is the sampled dataset; $|\Gamma|$ is the size of the dataset; and $\partial\Gamma$ is the subset of the sampled dataset, the spatial location of which is on the boundary $\partial\Omega$. The entire training process was optimized using the Adam optimizer to train the optimal set of weights $\tilde{\theta}$ for the neural network to minimize the total loss L (Xue et al., 2022b).

$$\tilde{\theta}=\underset{\theta}{\operatorname{argmin}}L(\theta) \tag{36}$$

In contrast to traditional data-driven approaches, an innovative HPDNN was constructed to obtain different field information by integrating physics-informed and data-driven neural networks, making it possible to train the model with only a small number of field samples and predict the values of arbitrary spatiotemporal parameters without solving the entire field. On the one hand, the proposed HPDNN does not require computation on each grid during training or prediction, similar to the gridless method. On the other hand, the HPDNN ensures that the prediction results strictly conform to the given constraints (e.g., governing equations, boundary conditions, and initial conditions) by embedding domain knowledge in the grid. However, in many scientific and field operations, some of the parameters of the model are poorly defined, and few measurements are available. Consequently, it is necessary to extrapolate hard-to-obtain parameters that describe the system from given measurements in order to more accurately predict model response—known as the inverse problem, i.e., reservoir parameter inversion. Inverting reservoir parameters by injection pressure dynamics requires solving a set of equations:

$$\tilde{\omega}=\underset{\omega}{\operatorname{argmin}}\sum_{x}\sum_{t}(\Phi(\boldsymbol{x},t,\omega,\tilde{\theta})-u(\boldsymbol{x},t))^2 \tag{37}$$

Therefore, under certain conditions, the inverse modeling problem can be understood as an optimization problem. Overall, the developed HPDNN can not only accurately predict the dynamic characteristics of CO_2 injection and evaluate the CO_2 sequestration potential, but also perform reservoir parameter inversion.

3. Results and discussion

3.1. Field application and model validation

After establishing the multi-scale CO_2 transport model, its field applicability must be checked using dynamic CO_2 injection data in the field. While operating the numerical model, the physical properties of reservoirs and CO_2 injection parameters were determined based on the actual CO_2 sequestration project in the Changlin-Weiyuan shale reservoir in the Sichuan Basin, China. Basic parameters can be obtained through detailed analysis of the core, fracturing operations, etc. The geometry and distribution of hydraulic fractures were determined by microseismic event. Thereafter, the CO_2 injection pressure difference was simulated using our model and comparisons were made between the simulation results and the field data. The fitting curves of the injection test data including the pressure difference (Δp_{w}) and pressure difference derivative ($\Delta p_{\mathrm{w}}'$) for the proposed model are shown in Fig. 5. As depicted in the figure, the simulation results of the proposed model are in good agreement with the field data, substantiating the reliability of our numerical model. The CO_2 transport characteristics of different scale media exist in the typical curves, which can be used to estimate the composition, structure, and properties of shale reservoirs and ultimately to evaluate the CO_2 sequestration capacity on the basis of the injection performance.

3.2. Results of the HPDNN model

In this section, the performance of the proposed HPDNN model was evaluated using stochastic CO_2 transport and sequestration cases to demonstrate the accuracy and robustness of the HPDNN model for different applications. The results of the proposed model are presented in detail from three aspects: prediction of injection dynamics, inversion of formation parameters, and evaluation of CO_2 sequestration capacity.

3.2.1. Prediction of CO_2 injection performance

The prediction results of the proposed HPDNN model on the CO_2 injection performance in depleted shale reservoirs based on data obtained from 500 sets of random numerical simulation operations are shown in Fig. 6. Fig. 6(a) and (b) constitute a comparison of prediction and simulation results of the pressure difference derivative curves at $t = 10^5$ h and $t = 10^2$ h, respectively, where the vertical axis is the Δp_{w} obtained from the simulation and the horizontal axis is the prediction result on the test set. The solid black slanted line in the figure is $y = x$; the closer the visible scatter point is to the solid black line, the higher is the fitting accuracy of the neural network. On this basis, the Pearson correlation coefficient (ρ) and goodness-of-fit (R^2) were used to further measure the fitting accuracy of the two groups of scattering sets; the closer the

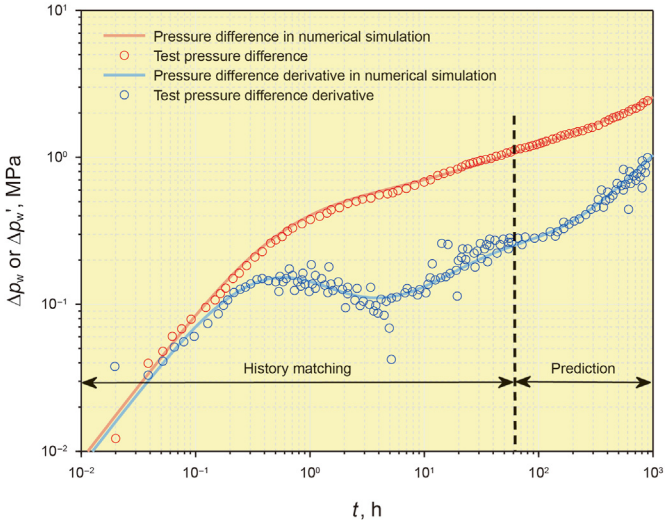

Fig. 5. Prediction results of the proposed CO_2 sequestration model in the field application.

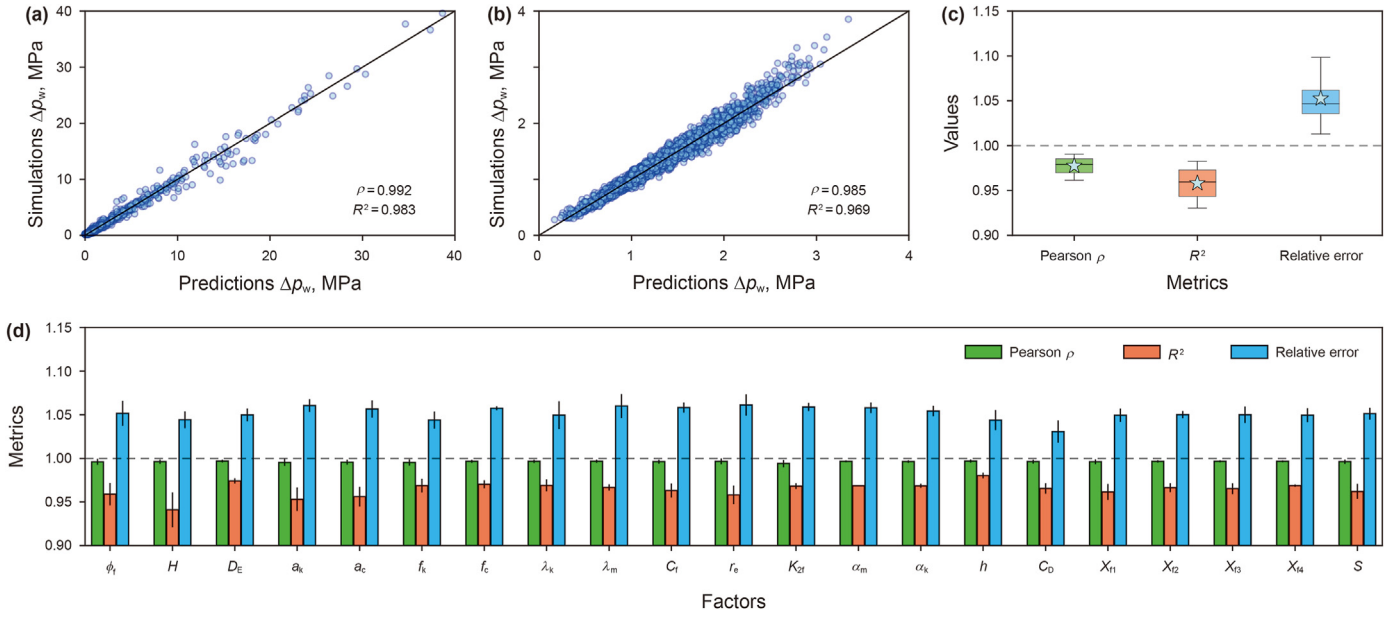

Fig. 6. Prediction performance of CO_2 injection dynamic curves of the HPDNN model.

two indicators were to 1, the higher the fitting accuracy of the neural network. The ρ and R^2 values of the deep learning model at different time points were 0.992, 0.983, 0.985, and 0.969, respectively, indicating that the fitting results of the CO_2 pressure injection dynamics were very accurate. The average fitting accuracy of the injection pressure predictions at all time points in the neural network is shown in Fig. 6(c). It is worth noting that the values at different times on the injection performance curves have significant numerical differences. Therefore, in addition to the Pearson correlation coefficient and goodness-of-fit, the relative error should be used to measure the performance of the neural network in the prediction of the CO_2 injection curves. To be closer in value to the above two indicators (convenient to display in one figure), one is added to the relative error; therefore, the closer the measurement result is to 1, the higher the prediction accuracy (the modified relative error is used by default to show the accuracy; no special statement will be made later). The average modified relative error (ε) is

$$\varepsilon = 1 + \frac{1}{n}\sum \frac{\left|y_{\text{pred}} - y_{\text{true}}\right|}{y_{\text{true}}} \tag{38}$$

It can be concluded from the prediction results that the HPDNN model has a high fitting accuracy at different times, indicating that the dynamic change in the injection curves can be well predicted. Furthermore, the single-parameter fitting accuracy of all input parameters was also evaluated, with the results shown in Fig. 6(d) where the black vertical bars represent $\pm$ 2 $\times$ SEM. Each main parameter was selected in turn as the target factor. The selected parameters were taken sequentially within a range of values of 100 equal points. In contrast, the remaining parameters that were not selected were taken as the mean value, resulting in 100 sets of test data for each parameter. It can be seen that the fitting results of the deep learning model on a single factor are also very accurate, indicating that our model can be used to analyze the influence of a single parameter on the injection performance curve or to infer the formation parameters and other tasks accurately.

The prediction results of the proposed model for the dynamic injection performance during CO_2 sequestration in depleted shale formations are shown in Fig. 7. There are four randomly selected prediction curves of CO_2 injection performance that contain subplots with local enlargement. The blue scatter lines represent the numerical simulation results and the red curves depict the prediction results of the HPDNN model. It is evident that the HPDNN model can accurately fit the injection dynamics of the numerical simulation operation, revealing excellent prediction performance. In addition, a comparison between the pressure fields obtained from the numerical simulations and those predicted by the HPDNN model for these two stochastic scenarios was performed. Three pairs of reservoir property parameters—H–λ_k, λ_m–f_k, and K_{2f}–r_e—were considered, all of which have more significant effects on the CO_2 transport processes in shale than other influencing factors. The value ranges of the parameters are $H \in [10^{-8}, 10^{-5}]$, $\lambda_k \in [10^{-6}, 10^{-4}]$, $\lambda_m \in [10^{-3}, 10^{-1}]$, and $r_e \in [1800, 20000]$, which are the values of uniform division under logarithmic coordinates; therefore, the horizontal and vertical coordinates of the pressure field are also in the order of logarithmic coordinates. It should be noted that—except for the two parameters currently under observation—the remaining parameters are taken as the logarithmic mean. The second, third, and fourth rows in Fig. 7 show the numerical simulation results, prediction results of the HPDNN model and the relative error between them, respectively. The Δp_w distribution results at two time points for each pair of parameters—t = 100 h (first column) and t = 4600 h (second column)—were investigated separately. It can be seen that the prediction results of the HPDNN model are consistent with the calculation results of the numerical simulation; furthermore, the relative error distribution diagram shows that the maximum relative error does not exceed 5% for any of the cases. In summary, our deep HPDNN and training strategy can efficiently and accurately predict and fit the computational results of actual numerical simulations, providing a powerful tool for two downstream tasks: (1) automatic inversion of reservoir parameters and (2) accurate assessment of CO_2 storage capacity.

3.2.2. Parameter inversion

The process of reservoir parameter inversion for shale with a multi-scale structure based on CO_2 injection performance was

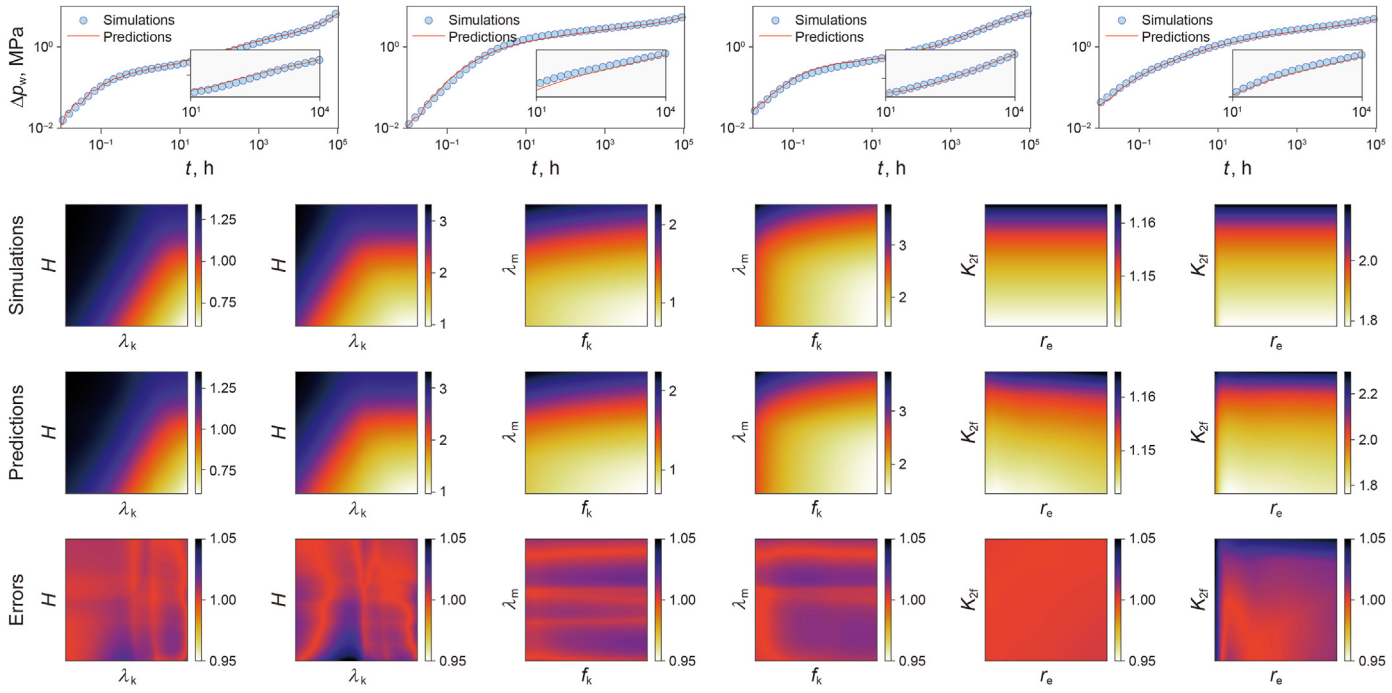

Fig. 7. The prediction accuracy results of the HPDNN model.

conducted as follows: (1) a set of reservoir parameters $\{\varphi_i\}$ was obtained based on geophysics, core analysis, and production testing; (2) the injection performance curves under the obtained parameters were calculated by numerical simulation and converted into the injection pressure vector in time and space $\{p_t\}$; and (3) the deep learning network is trained according to the pressure vector $\{p_t\}$ to invert the reservoir parameters that were close enough to the actual parameters $\{\varphi_i\}$. In addition, the value ranges of all parameters are not entirely free, as they each occupy a specific reasonable range. For example, the organic matter content is usually lower than 5% and the inter-porosity flow coefficient of porous kerogen (λ_k) is generally lower than that of matrix (λ_m). The optimization objective function is the difference between the predicted value of the deep learning network and the result of the numerical simulation based on the mean square error:

$$Loss = \frac{1}{n}\sum_t (p_t - \widehat{p}_t)^2 + \gamma \cdot \Phi(\widehat{p}|lims) \tag{39}$$

where $\Phi(\widehat{p}|lims)$ is the limit function and *lims* represents the preset range of parameter values, such that when the optimized variable $\widehat{p}_t$ jumps out of the predetermined range, Φ will impose a penalty on the objective function. To infer the input shale formation parameters, we used a trained neural network and froze its parameters. A set of initial input parameters was randomly generated, then the gradient descent method Adam was used to continuously optimize the input parameters to obtain the minimized error loss. To avoid multiple possible solutions and improve computational efficiency, it was important to use the target parameter set plus a larger interference to replace the completely random initial value.

Considering that the dynamic injection curves required in field applications of CO_2 storage in depleted shale reservoirs are usually not smooth and may be disturbed by various factors such as measurement and sampling errors, it is essential to examine the robustness of the parameter inversion method for field data containing different levels of noise. The performance of the reservoir parameter inversion portion of the HPDNN model was tested for the following three cases: (1) the original CO_2 injection pressure vector $\{p_t\}$ calculated by numerical simulation was taken as the input data; (2) the injection pressure vector $\{p_t\}$ plus a vector of uniformly distributed noise of ±10% was taken as the input data; and (3) the injection pressure vector $\{p_t\}$ plus a vector of uniformly distributed noise of ±20% was taken as the input data.

Using a randomly selected case in the test set as an example, the parameter inversion results of the HPDNN model for the observed data with different noise levels are shown in Fig. 8. The difference between the calculated and actual values of the reservoir parameters without noise in the injection performance is shown in Fig. 8(a). It can be seen that the deep learning algorithm has high accuracy in the inversion of reservoir parameters for this case, with an average relative error of 1.116 for all parameters. Random disturbances of 10% and 20% were then added to the injection dynamic data to generate datasets with different noise levels. On this basis, the parameters of the shale reservoir were inverted based on the dynamic injection curve with disturbance information; the statistical results of 100 realizations are shown in Fig. 8(b) and (c). It can be seen that the random interference of injected data affected the accuracy of reservoir parameter inversion to a certain extent. Specifically, the inversion accuracy of the algorithm for field data with more noise interference is lower. The average relative errors of all parameters in the two cases were 1.157 and 1.197, respectively. Moreover, it can be seen that the inversion difficulty of the factors H, λ_m, and λ_k was slightly larger than other parameters. In addition, future injection dynamics can be predicted based on the deduced values of the formation parameters. Therefore, a circular validation method can be used to demonstrate that the HPDNN can accurately relate the reservoir parameters to the dynamic injection performance. With the addition of different disturbances, the predicted CO_2 injection curves based on the inverted reservoir parameters are shown in Fig. 8(d), (e), and (f). It can be seen that the injection

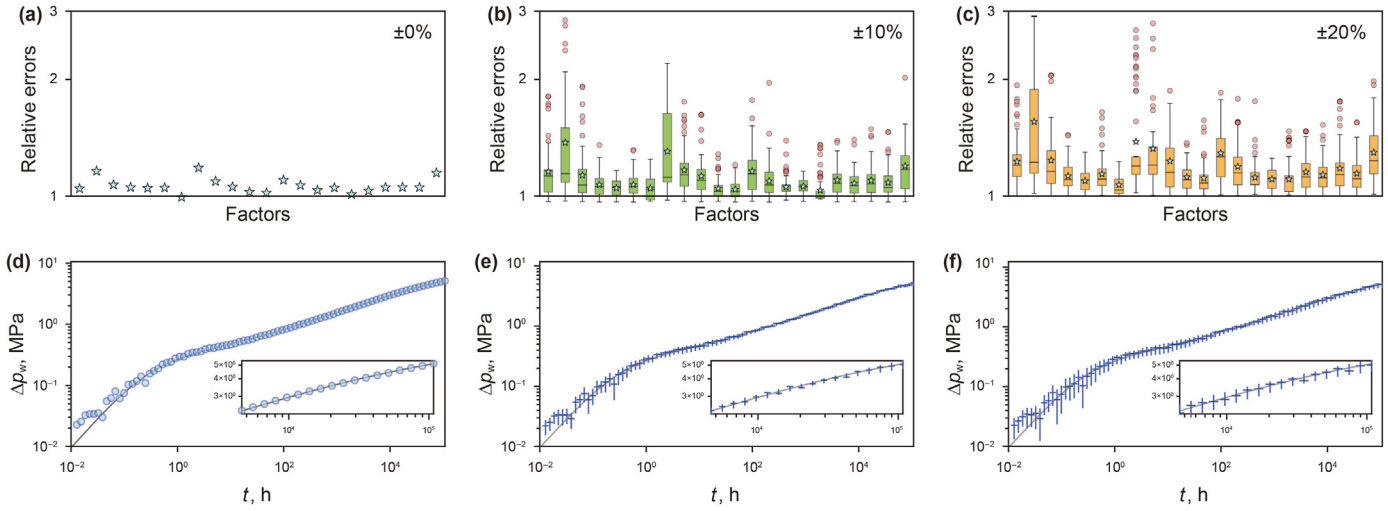

Fig. 8. Parameter inversion performance of the HPDNN model when noise exists (the sequence of factors is consistent with Fig. 6(d)).

dynamic curves predicted by using the parameters obtained by inversion were not significantly different than the real data, further confirming that the HPDNN model has strong robustness and an extensive applicability range when dealing with field data involving multiple noise sources.

The relative error results of the three cases based on 500 sets of numerical simulation data are shown in Fig. 9(a), (b), and (c), where each bar represents the average relative error of a parameter and the black implementation at the top of the bar represents 2 × SEM. When the result is closer to the innermost 1.0 dotted line, the parameter inversion of the algorithm is more accurate. It can be seen from the figure that the three dotted lines in the polar coordinate system represent relative errors of 1.0, 1.1, and 1.2, respectively. When there was no noise, results for the inversion of formation parameters were the most accurate. As the noise gradually increased, the average relative error and standard deviation of the mean gradually increased. However, the overall increase in relative error was slight, with the average relative error of all parameters at approximately 1.2—even under 20% noise—indicating that the model has a certain degree of robustness and can overcome the multi-noise problem of the injection pressure data in practical applications.

3.2.3. Evaluation of CO_2 sequestration capacity

Another essential function of the proposed HPDNN model was to determine the carbon sequestration potential of the target depleted shale formation based on the predicted injection performance. The CO_2 storage potential can be evaluated based on CO_2 injection rate and time obtained from the injection performance. To successfully predict the CO_2 sequestration capacity of the target depleted shale formation, we applied the following settings for the storage capacity prediction algorithm: given that the CO_2 injection pressure difference is usually significant, the minimum injection time corresponding to the minimum pressure difference was fixed at a constrained pressure that must be less than the fracture pressure of the shale reservoir; moreover, there is an intersection with the injection performance curve. Given that the range of injection pressure is not fixed under different reservoir parameters, regularized $\tilde{P}$ replaced P, with the relationship between the two represented as:

$$P^i = P^i_{\min} + \tilde{P} \cdot \left(P^i_{\max} - P^i_{\min}\right) \tag{40}$$

where P^i denotes the constrained injection pressure in case i; $P^i_{\min}$ and $P^i_{\max}$ are the minimum and maximum values of P^i, respectively.

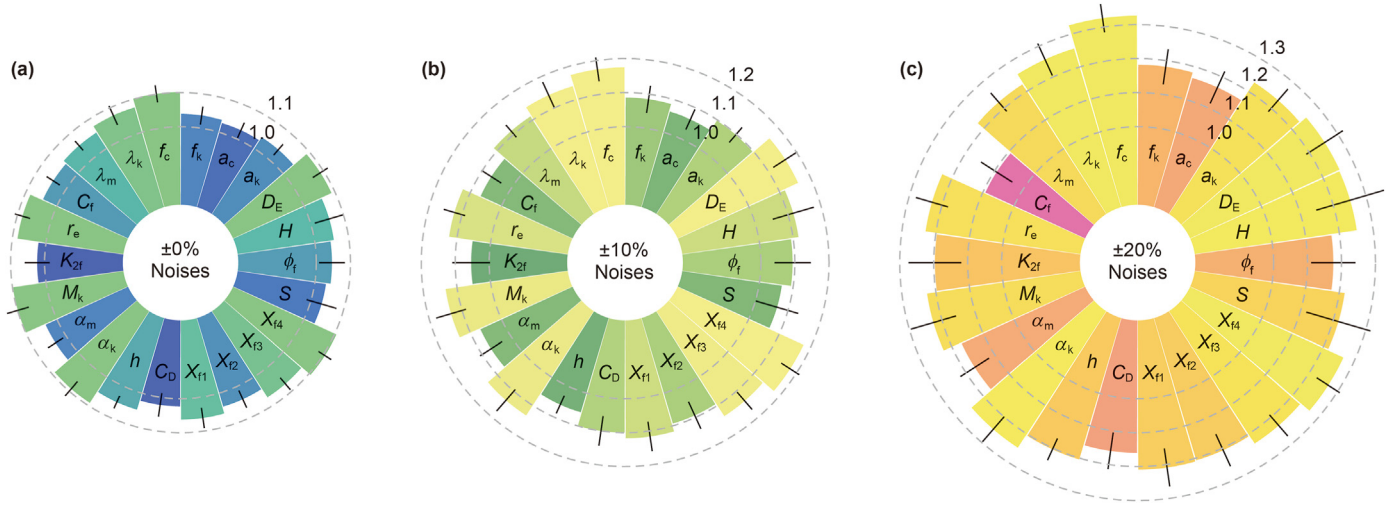

Fig. 9. The accuracy results of reservoir parameters inversion based on the HPDNN model.

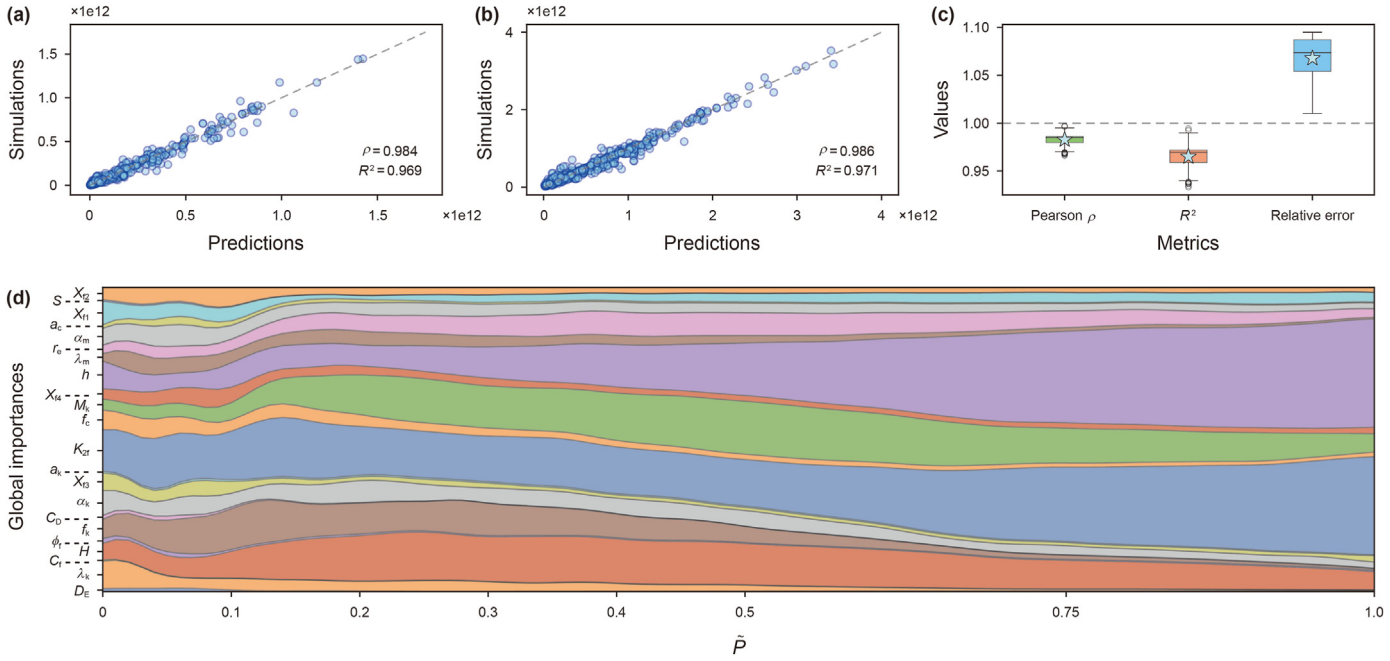

Fig. 10. Evaluation performance of CO_2 storage capacity of the HPDNN model.

The prediction results when $\tilde{P} = 0.5$ and 0.7 are shown in Fig. 10(a) and (b), respectively, using a total of 500 sets of simulated data as the test set; the closer the scatter position is to the black dashed line in the middle indicates the more accurate prediction of the algorithm. As depicted in the figure, the deep learning algorithm for predicting the CO_2 storage capacity is more accurate in both cases, with correlation coefficients ρ of 0.984 and 0.986 and R^2 of 0.969 and 0.971, respectively. The regularized injection pressure $\tilde{P}$ takes 1000 equal intervals in the range of [0,1]; therefore, for each $\tilde{P}$, the prediction accuracy can be measured using the test data. The statistical results for the prediction accuracy of CO_2 sequestration under different reservoir parameters and injection pressures are shown in Fig. 10(c). It can be seen that the three indicators are very close to 1.0, indicating that the deep learning algorithm has high accuracy in predicting levels of CO_2 sequestration and maintains excellent performance under different injection pressures.

To explore the applicability of the deep learning-based CO_2 sequestration model for different scenarios, a sensitivity analysis of the effects of the various basic parameters (including f_k, f_c, δ_c, δ_k, α_m, α_k, H, D_E, λ_m, λ_k, X_f, M_k, h, S, C_D, C_f, r_e) on the CO_2 sequestration capacity was conducted. The global importance of each factor in the model can also be calculated using the deep learning algorithm proposed in this study. The Sobol method was used to study the sensitivity of each reservoir parameter to CO_2 storage capacity using a trained neural network (Jia et al., 2022b). This can also be understood in terms of the influence of the parameters on the storage capacity: the greater the sensitivity, the more significant the impact of parameter changes on the final storage capacity. The global sensitivities of each parameter were calculated and normalized for all sensitivity values and the sensitivity results are shown in Fig. 10(d). It can be seen that with an increase in the normalized injection pressure $\tilde{P}$, the influence of the permeability K_{2f} of the outer zone and the reservoir thickness h on the CO_2 storage capacity gradually increased. K_{2f} and h of the depleted shale reservoir at $\tilde{P} = 1.0$ had a greater impact on the CO_2 storage capacity, because when a higher injection pressure was reached, the pressure wave was transmitted to the outer area of the reservoir. It can be concluded that the reservoir thickness and permeability of the outer zone throughout the well control area had a greater effect on CO_2 sequestration at higher constrained pressures. When $\tilde{P}$ was small, factors such as f_k, λ_k, λ_m, and H_D also had a greater impact on CO_2 sequestration levels. It can be concluded that the kerogen content, inter-porosity flow coefficients of inorganic matrix and kerogen, and effective diffusion coefficient had a more substantial effect on CO_2 storage capacity, indicating that these parameters should be prioritized when selecting shale sites for CO_2 storage. Comparatively, the impacts of the kerogen adsorption performance, clay content, slip flow coefficient, and other factors on the CO_2 storage capacity can be deprioritized based on their small-range variations. Furthermore, as the constrained pressure increased, the CO_2 storage capacity increased and the influence of various parameters on the capacity underwent constant change.

4. Conclusions

As a promising carbon reduction technology, CO_2 storage in depleted shale reservoirs is critical to alleviating the effects of greenhouse gases. In this study, a novel integrated model based on numerical simulation (COMSOL) was developed to precisely characterize the multiscale transport and sequestration processes. On this basis, a novel deep learning framework (HPDNN) applicable to practical prediction and decision making—specifically when addressing a significant amount of the fundamental parameters—was developed for CO_2 sequestration under complex scenarios. The HPDNN model incorporates scientific theories such as PDEs, engineering knowledge and expert experience, enabling deep learning to be driven not only by data from numerical simulations, but also by physical rules and engineering principles, thereby improving the accuracy, generalizability, and robustness of the model. By introducing the physical constraints, the proposed model can perfectly replace traditional laborious and time-consuming numerical simulations. Based on our verification and test results of the HPDNN model, the following conclusions can be drawn.

(1) A novel multiscale model of CO_2 storage in depleted shale formations, considering organic matter, porous kerogen, inorganic matrix, natural/hydraulic fractures, and SRV region, was developed and validated for multiple storage forms and transport mechanisms, including CO_2 diffusion, adsorption, dissolution, slip flow, and Darcy flow.
(2) Based on the proposed training strategy of integrating physical information, engineering theory, and observed data from numerical simulations, the HPDNN model efficiently and accurately fitted and predicted the injection performance and effectively discriminated the different transport processes of CO_2 in multi-scale systems of shale reservoirs.
(3) Drawing on the practice of history matching in traditional oilfield development and the fine-tuning technology of the neural network, the function of automatic reservoir parameter inversion in the HPDNN model was developed. Compared to the traditional parameter inversion method, this framework ensures higher accuracy, strong robustness, and an extensive applicability range when dealing with field data involving multiple noise sources.
(4) The HPDNN model also accurately determined the CO_2 storage capacity and performed a complex sensitivity analysis of the target depleted shale reservoir based on the physical characteristics obtained for the reservoir and engineering parameters applied, upon which field engineers is able to better control the CO_2 injection and choose a more suitable geo-structure for CO_2 storage engineering.
(5) This research is envisioned to bridge the basic system of knowledge on multi-scale transport processes and provide an indispensable basis for proceeding with the study of CO_2 geological sequestration in shale reservoirs. It is worth mentioning that multiphase fluid transport and CO_2-water-shale interaction are ignored in this study. Therefore, the proposed model will not be applicable when the mechanisms of multiphase fluid migration and water-rock reaction are dominant during the CO_2 storage in water-bearing shale gas reservoirs. Despite the limitations, the proposed model can still capture the main transport and storage mechanisms during CO_2 injection into depleted shale reservoirs. More importantly, compared with traditional methods, the proposed HPDNN can more intelligently predict injection performance, precisely perform reservoir parameter inversion, and reasonably evaluate CO_2 storage capacity under different conditions, thereby assisting engineers in formulating CO_2 sequestration plans in depleted shale formations more quickly and accurately.

Declaration of competing interest

The authors declare that they have no known competing financial interests or personal relationships that could have appeared to influence the work reported in this paper.

Acknowledgements

This work is funded by National Natural Science Foundation of China (Nos. 42202292, 42141011), the Program for Jilin University (JLU) Science and Technology Innovative Research Team (No. 2019TD-35). The authors would also like to thank the reviewers and editors whose critical comments are very helpful in preparing this article.

References

Afagwu, C., Abubakar, I., Kalam, S., et al., 2020. Pressure-transient analysis in shale gas reservoirs: a review. J. Nat. Gas Sci. Eng. 78, 103319. https://doi.org/10.1016/j.jngse.2020.103319.
Afagwu, C., Mahmoud, M.A., Alafnan, S., et al., 2022. Multiscale storage and transport modeling in unconventional shale gas: a review. J. Petrol. Sci. Eng. 208, 109518. https://doi.org/10.1016/j.petrol.2021.109518.
Alguliyev, R., Aliguliyev, R., Imamverdiyev, Y., et al., 2022. History matching of petroleum reservoirs using deep neural networks. Intelligent Systems with Applications 16, 200128. https://doi.org/10.1016/j.iswa.2022.200128.
Cai, M., Su, Y., Elsworth, D., et al., 2021. Hydro-mechanical-chemical modeling of sub-nanopore capillary-confinement on CO_2-CCUS-EOR. Energy 225, 120203. https://doi.org/10.1016/j.energy.2021.120203.
Cai, Z., Li, C., Wen, J., et al., 2022. Asset splitting algorithm for ultrahigh dimensional portfolio selection and its theoretical property. J. Econom. https://doi.org/10.1016/j.jeconom.2022.04.004.
Chen, S., Liu, J., Zhang, Q., et al., 2022. A critical review on deployment planning and risk analysis of carbon capture, utilization, and storage (CCUS) toward carbon neutrality. Renew. Sustain. Energy Rev. 167, 112537. https://doi.org/10.1016/j.rser.2022.112537.
Chen, X.W., Lin, X., 2014. Big data deep learning: challenges and perspectives. IEEE Access 2 (2), 514–525.
Chen, Z., Liu, Y., Sun, H., 2021. Physics-informed learning of governing equations from scarce data. Nat. Commun. 12 (1), 6136. https://doi.org/10.1038/s41467-021-26434-1.
Chu, H., Liao, X., Chen, Z., et al., 2019a. A new methodology to assess the maximum CO_2 geosequestration capacity of shale reservoirs with SRV based on wellbore pressure. J. CO_2 Util. 34, 239–255. https://doi.org/10.1016/j.jcou.2019.06.010.
Chu, H., Liao, X., Chen, Z., et al., 2019b. Estimating carbon geosequestration capacity in shales based on multiple fractured horizontal well: a case study. J. Petrol. Sci. Eng. 181, 106179. https://doi.org/10.1016/j.petrol.2019.06.043.
Chu, H., Dong, P., Lee, W.J., 2023. A deep-learning approach for reservoir evaluation for shale gas wells with complex fracture networks. Advances in Geo-Energy Research 7 (1), 49–65. https://doi.org/10.46690/ager.2023.01.06.
Chu, W., Zhang, K., 2023. Fluid phase behavior of tight and shale reservoirs: Monte Carlo simulations. Adv. Geo-Energy Res. 7 (2), 132–135. https://doi.org/10.46690/ager.2023.02.06.
Cui, R., Hassanizadeh, S.M., Sun, S., 2022. Pore-network modeling of flow in shale nanopores: network structure, flow principles, and computational algorithms. Earth Sci. Rev. 234, 104203. https://doi.org/10.1016/j.earscirev.2022.104203.
Dai, Z., Xu, L., Xiao, T., et al., 2020. Reactive chemical transport simulations of geologic carbon sequestration: methods and applications. Earth Sci. Rev. 208, 103265. https://doi.org/10.1016/j.earscirev.2020.103265.
Dong, P., Chen, Z., Liao, X., et al., 2022. Application of deep learning on well-test interpretation for identifying pressure behavior and characterizing reservoirs. J. Petrol. Sci. Eng. 208, 109264. https://doi.org/10.1016/j.petrol.2021.109264.
Feng, D., Li, X., Wang, X., et al., 2018. Capillary filling under nanoconfinement: the relationship between effective viscosity and water-wall interactions. Int. J. Heat Mass Tran. 118, 900–910. https://doi.org/10.1016/j.ijheatmasstransfer.2017.11.049.
Feng, Q., Xu, S., Xing, X., et al., 2020. Advances and challenges in shale oil development: a critical review. Advances in Geo-Energy Research 4 (4), 406–418. https://doi.org/10.46690/ager.2020.04.06.
Feng, D., Bakhshian, S., Wu, K., et al., 2021. Wettability effects on phase behavior and interfacial tension in shale nanopores. Fuel 290, 119983. https://doi.org/10.1016/j.fuel.2020.119983.
Gao, Q., Han, S., Cheng, Y., et al., 2022. Flow-coupled-geomechanical modelling of CO_2 transport in depleted shale from a microscopic perspective. Energy 257, 124727. https://doi.org/10.1016/j.energy.2022.124727.
Goodman, A., Sanguinito, S., Kutchko, B., et al., 2020. Shale pore alteration: potential implications for hydrocarbon extraction and CO_2 storage. Fuel 265, 116930. https://doi.org/10.1016/j.fuel.2019.116930.
Gou, Q., Xu, S., 2019. Quantitative evaluation of free gas and adsorbed gas content of Wufeng-Longmaxi shales in the Jiaoshiba area, Sichuan Basin, China. Advances in Geo-Energy Research 3 (3), 258–267. https://doi.org/10.26804/ager.2019.03.04.
He, J., Teng, W., Xu, J., et al., 2016. A quadruple-porosity model for shale gas reservoirs with multiple migration mechanisms. J. Nat. Gas Sci. Eng. 33, 918–933. https://doi.org/10.1016/j.jngse.2016.03.059.
Hourfar, F., Bidgoly, H.J., Moshiri, B., et al., 2019. A reinforcement learning approach for waterflooding optimization in petroleum reservoirs. Eng. Appl. Artif. Intell. 77, 98–116. https://doi.org/10.1016/j.engappai.2018.09.019.
Huang, L., Zhou, W., Xu, H., et al., 2021. Dynamic fluid states in organic-inorganic nanocomposite: implications for shale gas recovery and CO_2 sequestration. Chem. Eng. J. (Lausanne) 411, 128423. https://doi.org/10.1016/j.cej.2021.128423.
Iddphonce, R., Wang, J., Zhao, L., 2020. Review of CO_2 injection techniques for enhanced shale gas recovery: prospect and challenges. J. Nat. Gas Sci. Eng. 77, 103240. https://doi.org/10.1016/j.jngse.2020.103240.
Javadpour, F., Singh, H., Rabbani, A., et al., 2021. Gas flow models of shale: a review. Energy Fuel. 35 (4), 2999–3010. https://doi.org/10.1021/

acs.energyfuels.0c04381.
Jeffry, L., Ong, M.Y., Nomanbhay, S., et al., 2021. Greenhouse gases utilization: a review. Fuel 301, 121017. https://doi.org/10.1016/j.fuel.2021.121017.
Jeon, P.R., Choi, J., Yun, T.S., et al., 2014. Sorption equilibrium and kinetics of CO_2 on clay minerals from subcritical to supercritical conditions: CO_2 sequestration at nanoscale interfaces. Chem. Eng. J. (Lausanne) 255, 705–715. https://doi.org/10.1016/j.cej.2014.06.090.
Jia, B., Chen, Z., Xian, C., 2022a. Investigations of CO_2 storage capacity and flow behavior in shale formation. J. Petrol. Sci. Eng. 208, 109659. https://doi.org/10.1016/j.petrol.2021.109659.
Jia, B., Tsau, J.-S., Barati, R., 2019. A review of the current progress of CO_2 injection EOR and carbon storage in shale oil reservoirs. Fuel 236, 404–427. https://doi.org/10.1016/j.fuel.2018.08.103.
Jia, S., Dai, Z., Yang, Z., et al., 2022b. Uncertainty quantification of radionuclide migration in fractured granite. J. Clean. Prod. 366, 132944. https://doi.org/10.1016/j.jclepro.2022.132944.
Karniadakis, G.E., Kevrekidis, I.G., Lu, L., et al., 2021. Physics-informed machine learning. Nature Reviews Physics 3 (6), 422–440. https://doi.org/10.1038/s42254-021-00314-5.
Klewiah, I., Berawala, D.S., Alexander Walker, H.C., et al., 2020. Review of experimental sorption studies of CO_2 and CH_4 in shales. J. Nat. Gas Sci. Eng. 73, 103045. https://doi.org/10.1016/j.jngse.2019.103045.
Kou, Z., Wang, T., Chen, Z., et al., 2021. A fast and reliable methodology to evaluate maximum CO_2 storage capacity of depleted coal seams: a case study. Energy 231, 120992. https://doi.org/10.1016/j.energy.2021.120992.
Kou, Z., Zhang, D., Chen, Z., et al., 2022. Quantitatively determine CO_2 geo-sequestration capacity in depleted shale reservoir: a model considering viscous flow, diffusion, and adsorption. Fuel 309, 122191. https://doi.org/10.1016/j.fuel.2021.122191.
Li, C., Li, R., Wen, J., et al., 2022a. Regularized linear programming discriminant rule with folded concave penalty for ultrahigh-dimensional data. J. Comput. Graph Stat. 1–9. https://doi.org/10.1080/10618600.2022.2143785.
Li, H., Misra, S., 2021. Reinforcement learning based automated history matching for improved hydrocarbon production forecast. Appl. Energy 284, 116311. https://doi.org/10.1016/j.apenergy.2020.116311.
Li, Y., Zhou, Z., Ying, S., 2022b. DeLISA: deep learning based iteration scheme approximation for solving PDEs. J. Comput. Phys. 451, 110884. https://doi.org/10.1016/j.jcp.2021.110884.
Liehui, Z., Baochao, S., Yulong, Z., et al., 2019. Review of micro seepage mechanisms in shale gas reservoirs. Int. J. Heat Mass Tran. 139, 144–179. https://doi.org/10.1016/j.ijheatmasstransfer.2019.04.141.
Liu, Y.-Y., Ma, X.-H., Zhang, X.-W., et al., 2021. A deep-learning-based prediction method of the estimated ultimate recovery (EUR) of shale gas wells. Petrol. Sci. 18 (5), 1450–1464. https://doi.org/10.1016/j.petsci.2021.08.007.
Lucas, S., Calvo, M.P., Palencia, C., et al., 2004. Mathematical model of supercritical CO_2 adsorption on activated carbon: effect of operating conditions and adsorption scale-up. J. Supercrit. Fluids 32 (1), 193–201. https://doi.org/10.1016/j.supflu.2004.02.008.
Lyu, Q., Tan, J., Li, L., et al., 2021. The role of supercritical carbon dioxide for recovery of shale gas and sequestration in gas shale reservoirs. Energy Environ. Sci. 14 (8), 4203–4227. https://doi.org/10.1039/d0ee03648j.
Mao, Z., Jagtap, A.D., Karniadakis, G.E., 2020. Physics-informed neural networks for high-speed flows. Comput. Methods Appl. Mech. Eng. 360, 112789. https://doi.org/10.1016/j.cma.2019.112789.
Mora, C., Spirandelli, D., Franklin, E.C., et al., 2018. Broad threat to humanity from cumulative climate hazards intensified by greenhouse gas emissions. Nat. Clim. Change 8 (12), 1062–1071. https://doi.org/10.1038/s41558-018-0315-6.
Najafabadi, M.M., Villanustre, F., Khoshgoftaar, T.M., et al., 2015. Deep learning applications and challenges in big data analytics. Journal of Big Data 2 (1), 1. https://doi.org/10.1186/s40537-014-0007-7.
Nicolas, V., Sdanghi, G., Mozet, K., et al., 2022. Numerical simulation of a thermally driven hydrogen compressor as a performance optimization tool. Appl. Energy 323, 119628. https://doi.org/10.1016/j.apenergy.2022.119628.
Peng, X., Rao, X., Zhao, H., et al., 2022. A proxy model to predict reservoir dynamic pressure profile of fracture network based on deep convolutional generative adversarial networks (DCGAN). J. Petrol. Sci. Eng. 208, 109577. https://doi.org/10.1016/j.petrol.2021.109577.
Raissi, M., Perdikaris, P., Karniadakis, G.E., 2019. Physics-informed neural networks: a deep learning framework for solving forward and inverse problems involving nonlinear partial differential equations. J. Comput. Phys. 378, 686–707. https://doi.org/10.1016/j.jcp.2018.10.045.
Raissi, M., Yazdani, A., Karniadakis, G.E., 2020. Hidden fluid mechanics: learning velocity and pressure fields from flow visualizations. Science 367 (6481), 1026–1030. https://doi.org/10.1126/science.aaw4741.
Ray, P., Reddy, S.S., Banerjee, T., 2021. Various dimension reduction techniques for high dimensional data analysis: a review. Artif. Intell. Rev. 54 (5), 3473–3515. https://doi.org/10.1007/s10462-020-09928-0.
Shen, X., Liu, H., Mu, L., et al., 2023. A semi-analytical model for multi-well leakage in a depleted gas reservoir with irregular boundaries. Gas Science and Engineering 114, 204979. https://doi.org/10.1016/j.jgsce.2023.204979.
Shen, X., Liu, H., Zhang, Y., et al., 2022. An integrated model for carbon geo-sequestration considering gas leakage. J. Petrol. Sci. Eng. 217, 110899. https://doi.org/10.1016/j.petrol.2022.110899.
Steiner, T.R., 2022. High temperature steady-state experiment for computational radiative heat transfer validation using COMSOL and ANSYS. Results in Engineering 13, 100354. https://doi.org/10.1016/j.rineng.2022.100354.
Sun, Z., Li, X., Liu, W., et al., 2020. Molecular dynamics of methane flow behavior through realistic organic nanopores under geologic shale condition: pore size and kerogen types. Chem. Eng. J. (Lausanne) 398, 124341. https://doi.org/10.1016/j.cej.2020.124341.
Tang, Y., Fan, J., Li, X., et al., 2022. Physics-informed recurrent neural network for time dynamics in optical resonances. Nature Computational Science 2 (3), 169–178. https://doi.org/10.1038/s43588-022-00215-2.
Tayari, F., Blumsack, S., 2020. A real options approach to production and injection timing under uncertainty for CO_2 sequestration in depleted shale gas reservoirs. Appl. Energy 263, 114491. https://doi.org/10.1016/j.apenergy.2020.114491.
Wang, H., Chen, L., Qu, Z., et al., 2020. Modeling of multi-scale transport phenomena in shale gas production — a critical review. Appl. Energy 262, 114575. https://doi.org/10.1016/j.apenergy.2020.114575.
Wang, S., Qin, C., Feng, Q., et al., 2021a. A framework for predicting the production performance of unconventional resources using deep learning. Appl. Energy 295, 117016. https://doi.org/10.1016/j.apenergy.2021.117016.
Wang, Y., Dai, Z., Chen, L., et al., 2023. An integrated multi-scale model for CO_2 transport and storage in shale reservoirs. Appl. Energy 331, 120444. https://doi.org/10.1016/j.apenergy.2022.120444.
Wang, Y., Dai, Z., Liu, H., 2021b. Pore-scale mechanisms and simulations for gas–water two-phase transport processes in natural gas reservoirs. J. Nat. Gas Sci. Eng. 96, 104314. https://doi.org/10.1016/j.jngse.2021.104314.
Wang, Y., Liu, H., Guo, M., et al., 2021c. Image recognition model based on deep learning for remaining oil recognition from visualization experiment. Fuel 291, 120216. https://doi.org/10.1016/j.fuel.2021.120216.
Wang, Y., Liu, H., Zhou, Y., 2021d. Development of a deep learning-based model for the entire production process of steam-assisted gravity drainage (SAGD). Fuel 287, 119565. https://doi.org/10.1016/j.fuel.2020.119565.
Wen, J., Yang, S., Wang, C.D., et al., 2023. Feature-splitting algorithms for ultrahigh dimensional quantile regression. J. Econom. https://doi.org/10.1016/j.jeconom.2023.01.028.
Wu, H., Qiao, R., 2021. Physics-constrained deep learning for data assimilation of subsurface transport. Energy and AI 3, 100044. https://doi.org/10.1016/j.egyai.2020.100044.
Xiao, K., Yu, B., Cheng, L., et al., 2022. The effects of CCUS combined with renewable energy penetration under the carbon peak by an SD-CGE model: evidence from China. Appl. Energy 321, 119396. https://doi.org/10.1016/j.apenergy.2022.119396.
Xie, Q., Wang, W., Su, Y., et al., 2023. Pore-scale study of calcite dissolution during CO_2-saturated brine injection for sequestration in carbonate aquifers. Gas Science and Engineering 114, 204978. https://doi.org/10.1016/j.jgsce.2023.204978.
Xu, S., Ren, G., Younis, R.M., et al., 2021a. Revisiting field estimates for carbon dioxide storage in depleted shale gas reservoirs: the role of geomechanics. Int. J. Greenh. Gas Control 105, 103222. https://doi.org/10.1016/j.ijggc.2020.103222.
Xu, W.-J., Xu, Q., Liu, G.-Y., et al., 2021b. A novel parameter inversion method for an improved DEM simulation of a river damming process by a large-scale landslide. Eng. Geol. 293, 106282. https://doi.org/10.1016/j.enggeo.2021.106282.
Xue, L., Gu, S., Mi, L., et al., 2022a. An automated data-driven pressure transient analysis of water-drive gas reservoir through the coupled machine learning and ensemble Kalman filter method. J. Petrol. Sci. Eng. 208, 109492. https://doi.org/10.1016/j.petrol.2021.109492.
Xue, Y., Tong, Y., Neri, F., 2022b. An ensemble of differential evolution and Adam for training feed-forward neural networks. Inf. Sci. 608, 453–471. https://doi.org/10.1016/j.ins.2022.06.036.
Yan, J., Zhang, Z., 2019. Carbon capture, utilization and storage (CCUS). Appl. Energy 235, 1289–1299. https://doi.org/10.1016/j.apenergy.2018.11.019.
Yang, S., Wen, J., Zhan, X., et al., 2019. ET-Lasso: a new efficient tuning of lasso-type regularization for high-dimensional data. In: The 25th ACM SIGKDD International Conference.
Yang, Y., Hou, M., Sun, H., et al., 2020. Neural network algorithm based on Legendre improved extreme learning machine for solving elliptic partial differential equations. Soft Comput. 24 (2), 1083–1096. https://doi.org/10.1007/s00500-019-03944-1.
Zhan, C., Dai, Z., Samper, J., et al., 2022. An integrated inversion framework for heterogeneous aquifer structure identification with single-sample generative adversarial network. J. Hydrol. 610, 127844. https://doi.org/10.1016/j.jhydrol.2022.127844.
Zhang, T., Zhang, B.N., Zhao, Y.L., et al., 2022a. Simulation of water flow in a nanochannel with a sudden contraction or expansion. Langmuir 38 (21), 6720–6730. https://doi.org/10.1021/acs.langmuir.2c00672.
Zhang, T., Zhang, L., Zhao, Y., et al., 2022b. Ganglia dynamics during imbibition and drainage processes in nanoporous systems. Phys. Fluids 34 (4). https://doi.org/10.1063/5.0089950.
Zhang, T., Luo, S., Zhou, H., et al., 2023. Pore-scale modelling of water sorption in nanopore systems of shale. Int. J. Coal Geol. 273, 104266. https://doi.org/10.1016/j.coal.2023.104266.
Zhou, J., Hu, N., Xian, X., Zhou, L., Tang, J., Kang, Y., Wang, H., 2019. Supercritical CO_2 fracking for enhanced shale gas recovery and CO_2 sequestration: results, status and future challenges. Adv. Geo-Energy Res. 3 (2), 207–224. https://doi.org/10.26804/ager.2019.02.10.
Zhou, Y., Wang, Y., 2022. An integrated framework based on deep learning algorithm for optimizing thermochemical production in heavy oil reservoirs. Energy 253, 124140. https://doi.org/10.1016/j.energy.2022.124140.